A Case Study of Cloud-Top Kelvin–Helmholtz Instability Waves near the Dendritic Growth Zone

M. D. CANN,[a] K. FRIEDRICH,[a] J. R. FRENCH,[b] AND D. BEHRINGER[b]

[a] *Department of Atmospheric and Oceanic Sciences, University of Colorado Boulder, Boulder, Colorado*
[b] *Department of Atmospheric Science, University of Wyoming, Laramie, Wyoming*

(Manuscript received 16 April 2021, in final form 9 November 2021)

ABSTRACT: Kelvin–Helmholtz instability (KH) waves have been broadly shown to affect the growth of hydrometeors within a region of falling precipitation, but formation and growth from KH waves at cloud top needs further attention. Here, we present detailed observations of cloud-top KH waves that produced a snow plume that extended to the surface. Airborne transects of cloud radar aligned with range height indicator scans from ground-based precipitation radar track the progression and intensity of the KH wave kinetics and precipitation. In situ cloud probes and surface disdrometer measurements are used to quantify the impact of the snow plume on the composition of an underlying supercooled liquid water (SLW) cloud and the snowfall observed at the surface. KH wavelengths of 1.5 km consisted of ~750-m-wide up- and downdrafts. A distinct fluctus region appeared as a wave-breaking cloud top where the fastest updraft was observed to exceed 5 m s^{-1}. Relatively weaker updrafts of 0.5–1.5 m s^{-1} beneath the fluctus and partially overlapping the dendritic growth zone were associated with steep gradients in reflectivity of -5 to 20 dBZ_e in as little as 500-m depths due to rapid growth of pristine planar ice crystals. The falling snow removed ~80% of the SLW content from the underlying cloud and led to a twofold increase in surface liquid equivalent snowfall rate from 0.6 to 1.3 mm h^{-1}. This paper presents the first known study of cloud-top KH waves producing snowfall with observations of increased snowfall rates at the surface.

KEYWORDS: Kelvin-Helmholtz instabilities; Clouds; Snowfall; Aircraft observations; In situ atmospheric observations; Radars/Radar observations

1. Introduction

Kelvin–Helmholtz instability (hereafter KH) waves and their microphysical impacts are well documented *within* falling precipitation, but observations of KH waves at cloud top are extremely scarce and their impacts on clouds and precipitation have yet to be characterized. Past studies have identified that KH waves within precipitation can enhance growth and fallout of hydrometeors through increased aggregation, accretion, coalescence, and vapor deposition (Houze and Medina 2005; Houser and Bluestein 2011; Medina and Houze 2016; Barnes et al. 2018). However, the microphysical impacts from KH waves within a cloud are distinctly different from cloud-top KH waves. KH waves within a cloud act to enhance growth of existing hydrometeors whereas cloud-top KH waves are associated with the formation of precipitation-sized hydrometeors. Hydrometeor formation from cloud-top KH waves can have implications for underlying clouds and precipitation at the surface. Here, we present a study of cloud-top KH waves that generated ice crystals which fell through an underlying orographic cloud containing supercooled liquid water (SLW) and led to enhanced snowfall at the surface. The analysis uses data from cloud and precipitation radars, in situ measurements of particle size and concentration, and surface optical disdrometer measurements. The data presented herein are from an intensive observation period (IOP) during the Seeded and Natural Orographic Wintertime Clouds: The Idaho Experiment (SNOWIE; Tessendorf et al. 2019) conducted in the Payette Mountains of Idaho during an 8-week period in winter 2017.

KH waves are ubiquitous in the troposphere both in dry air (Atlas et al. 1970; Browning and Watkins 1970; Keller 1990; Jaeger and Sprenger 2007) and within precipitating systems such as convection, frontal boundaries, and midlatitude cyclones (Petre and Verlinde 2004; Friedrich et al. 2008; Geerts and Miao 2010; Marsham et al. 2010; Houser and Bluestein 2011; Browning et al. 2012; Aikins et al. 2016; Medina and Houze 2016; Barnes et al. 2018; Grasmick and Geerts 2020). The KH waves form via dynamic instability in the presence of strong vertical wind shear, weak static stability, or both. When the shear-squared magnitude exceeds the buoyancy magnitude by a factor of 4, atmospheric layers have a Richardson number (Ri) less than 0.25 and can generate KH waves (e.g., Miles and Howard 1964; Turner 1973; Houze and Medina 2005). Layers of shear often exist across airmass boundaries but are also found in orographic flow (Grasmick and Geerts 2020). A composite rawinsonde analysis from all 24 SNOWIE IOPs suggests that KH wave formation in saturated air was possible in ~60% of sampled atmospheres from the surface to 8 km MSL in the Payette Mountains of Idaho (Cann and Friedrich 2020). Regardless of altitude, when KH waves exist in subfreezing temperatures, the dominant mechanism for microphysical growth was suggested to be increased aggregation along the region of upward motion (Barnes et al. 2018). At temperatures of $-7°$ to 0°C, riming promotes hydrometeor growth (Houser and Bluestein 2011; Barnes et al. 2018), including the splintering of ice crystals near -5°C

Corresponding author: Matthew D. Cann, matthew.cann@colorado.edu

DOI: 10.1175/JAS-D-21-0106.1

(Hallett and Mossop 1974), leading to rapid production of needles (Houser and Bluestein 2011).

Ice crystal growth and microphysical processes affected by KH wave kinetics can be studied with dual-polarization precipitation radar (e.g., Houser and Bluestein 2011; Barnes et al. 2018). Dual polarization radar provides equivalent reflectivity factor Z_e, differential reflectivity Z_{DR}, specific differential phase K_{DP}, and copolar correlation coefficient ρ_{hv}, which yield valuable information on particle shape, size, and distribution (e.g., Ryzhkov and Zrnić 1998; Kumjian 2013a). These dual-polarization variables are particularly useful for identifying planar crystals like dendrites, which are highly efficient at aggregation and form most commonly at temperatures between −12° and −18°C (the dendritic growth zone, DGZ) with a maximum occurrence around −15°C (Libbrecht 2005; Bailey and Hallett 2009; Kennedy and Rutledge 2011; Bechini et al. 2013). Plates, another planar crystal, tend to grow at temperatures at the periphery of the DGZ, common in temperatures between −8° and −12°C, and −18° and −20°C (Bailey and Hallett 2009). In addition to ambient temperature, the formation of particular ice species, such as dendrites and sector plates, is dependent on ice supersaturation (see Bailey and Hallett 2009, their Fig. 5). Previously, planar ice crystals have been identified from dual-polarization variables when $1 < Z_{\mathrm{DR}} < 5$ dB, $K_{\mathrm{DP}} > 0.25°\ \mathrm{km}^{-1}$, and $0.95 < \rho_{\mathrm{hv}} < 0.99$ (e.g., Ryzhkov and Zrnić 1998; Kennedy and Rutledge 2011; Andrić et al. 2013; Bechini et al. 2013; Kumjian 2013a,b; Schneebeli et al. 2013; Schrom et al. 2015; Trömel et al. 2019). The high values of Z_{DR} and K_{DP} are the result of planar structure of ice crystals, which in a bulk sense are oriented parallel to the horizontal radar polarization. However, individual crystals tend to flutter as they fall, causing reduced ρ_{hv} in regions of pristine ice crystals. As ice crystals begin to aggregate, Z_{DR} decreases toward 0 and ρ_{hv} becomes closer to 1, whereas K_{DP} remains $>0.25°\ \mathrm{km}^{-1}$ if a mix of pristine planar crystals and aggregates exists (Kumjian 2013a). A transition to larger Z_e and slightly positive Z_{DR} is indicative of aggregates due to their low density and particle fluttering, whereas Z_{DR} in rimed ice crystals, or graupel, tends to exhibit slightly negative Z_{DR} and K_{DP} as conical shapes are produced and vertically oriented (Kumjian 2013a; Oue et al. 2015; Schrom and Kumjian 2016; Bringi et al. 2017).

In this study, we aim to address the following questions:

1) How are cloud-top KH wave kinetics linked to the formation and growth of ice crystals within the wave structure?
2) How does the ice introduced by the KH waves affect the composition of the underlying SLW cloud?
3) How do cloud-top KH waves impact precipitation at the ground?

The paper is organized to describe the observational tools and methods used to analyze the event in section 2. A brief case overview is described in section 3. We identify and document the progression of the KH wave train in section 4. We present a comprehensive analysis on the KH wave kinetic–microphysical linkages in section 5. The cloud and surface in situ analyses are presented in section 6. We draw conclusions in section 7.

2. Observations and methods

a. *UWKA Wyoming Cloud Radar and in situ probes*

The Wyoming Cloud Radar (WCR; Wang et al. 2012) is a W-band polarimetric Doppler radar that, for this study, used two fixed, vertically oriented antennas (near-zenith, near-nadir) providing 15–30-m resolution at 1 km. The WCR measures Z_e and Doppler velocity, from the surface to ~10 km. After aircraft motion removal (Leon and Vali 1998), the processed Doppler velocity is a combination of the vertical air velocity, reflectivity-weighted hydrometeor fall velocity, and some small contribution of the horizontal wind due to deviations from vertical of the radar beams. We confine our analysis to straight and level flight. Removing an assumed 1 m s^{-1} fall speed of snow, the remaining is an *estimate* of the air vertical velocity (w). The maximum bias/error resulting from this assumption depends on the species of crystals and the degree of riming and will generally be between about 0.5 m s^{-1} upward to 1 m s^{-1} downward. The assumption is most appropriate for unrimed to lightly rimed ice crystals such as plates, dendrites, and columns that exceed 1-mm diameter. Smaller crystals and completely unrimed plates and dendrites generally have fall velocities between 0.5 and 0.75 m s^{-1}, resulting in positive (upward) bias of 0.25–0.5 m s^{-1}. Heavily rimed ice, especially columns and needles, can have fall velocities of 2 m s^{-1} or more and result in negative (downward) bias of ~1 m s^{-1}. However, densely rimed dendrites tend to fall around 1 m s^{-1}, therefore we expect little bias for such cases (Mitchell 1996; Barthazy and Schefold 2006).

In situ probes on the UWKA measured cloud- and precipitation-sized particles and bulk liquid and ice content along the aircraft track. The Cloud Droplet Probe (CDP) provides concentration of cloud droplets with diameters from 2 to 50 μm in 27 size bins. Details of the CDP operating principals, limitations, and calibration for the UWKA are provided by Lance et al. (2010) and Faber et al. (2018). Larger hydrometeors with diameters from ~10 μm to ~10 mm were sampled using two optical array probes, a two-dimensional stereo (2D-S; Lawson et al. 2006) and two-dimensional precipitation (2D-P; Knollenberg 1970) probes. Images from these probes were processed using the University of Illinois Optical Array Probe Processing Software (Jackson et al. 2014; Finlon et al. 2016) and size distributions and number concentrations were computed for each 1 s of flight data. For the combined size distributions presented herein, data from the CDP were used for 2–50 μm, from the 2D-S for 50–1000 μm, and from the 2D-P for >1 mm. Visual characterization of images were used to determine the ice crystal habit in the sampled regions within the cloud. These images aid in evaluating the microphysical processes of growing ice crystals and were used together with dual-polarization radar measurements to diagnose such processes.

Bulk liquid water content (LWC) and total water content (TWC, liquid plus ice) were measured using a hot-wire deep-cone Nevzorov probe (Korolev et al. 1998, 2013). Processing of the Nevzorov data included manual baseline adjustments in regions where significant riming of the sensing elements occurs. Both LWC and TWC are sensitive to ~0.02 g m^{-3},

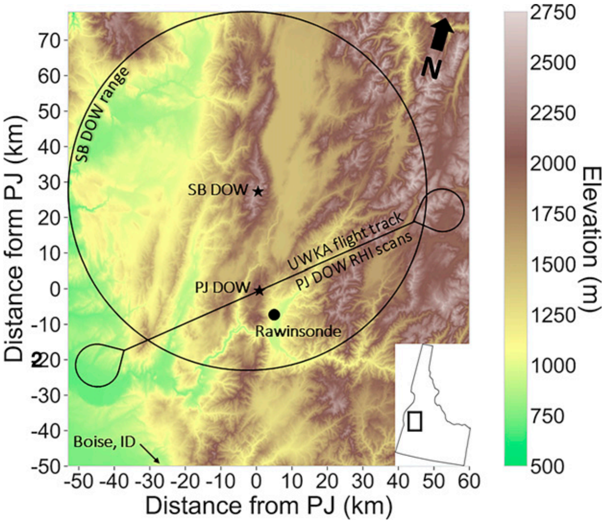

FIG. 1. SNOWIE domain and operations for IOP04 on 18 Jan 2017 in the Payette Mountains of Idaho, just north of Boise. The UWKA flight track and PJ DOW RHI scans are aligned on the same 235°–55°-oriented transect.

and uncertainties in the measurements are estimated to be ~10% (Baumgardner et al. 2017).

b. Doppler on wheels X-band dual-polarization Doppler radar

Two Doppler on Wheels (DOW) X-band dual-polarization Doppler radars were deployed to the summits of Snowbank (hereafter SB DOW; 2542 m MSL; Fig. 1b) and Packer John Mountains (hereafter PJ DOW; 2138 m MSL; Fig. 1b). The DOWs' range resolution was set at 50 m, with a maximum range of 50 km. Dual-polarization from the DOWs return Z_e, Z_{DR}, differential propagation phase ϕ_{DP}, and ρ_{hv}. During the passage of KH waves the DOWs were employing two different scan strategies that are described below. The scan strategy for both radars is shown in Table 1. The 235°–55° range–height indicator (RHI) pair matches the flight path of the UWKA and has ~1-min delay between scans. Given the short time lag between scans, we matched upwind scans with their downwind counterparts to provide a 100-km composite transect across the Payette Mountains.

Both DOWs were subject to calibration scans, postprocessing, and decluttering of the radar fields (Tessendorf et al. 2019; Friedrich et al. 2020). After SNOWIE, the DOWs were collocated with the KFTG WSR-88D radar near Denver, CO and using comparisons of 1° elevation scans calculated a Z_e offset of +3.4 (7.6) ± 1 dBZ_e for the SB DOW and +7.6 ± 1 dBZ_e for the PJ DOW. The calibrated data were then used to remove ground clutter and other nonprecipitating echoes using a fuzzy logic algorithm adapted from Gourley et al. (2007) and following the method of Aikins et al. (2016). The method compares radar retrieved fields of Z_{DR}, ϕ_{DP}, and ρ_{hv} to known density functions of precipitating and nonprecipitating echoes to characterize and remove the nonprecipitating echoes.

c. Rawinsondes, micro rain radar, and PARSIVEL disdrometer

A Lockheed Martin Sippican LMS-6 rawinsonde launched at 2200 UTC with a vertical resolution of 10 m was used to calculate the squared moist Brunt–Väisälä frequency $\left(N_m^2\right)$ following Lalas and Einaudi (1974), Durran and Klemp (1982), and Hughes et al. (2009):

$$N_m^2 = \left[\frac{g}{T}\left(\frac{dT}{dz} + \Gamma_m\right)\left(1 + \frac{Lr_s}{R_d T}\right) - \frac{g}{1 + r_s}\frac{dr_s}{dz}\right], \qquad (1)$$

where g is gravity (9.81 m s^{-1}), T is temperature, Γ_m is the moist-adiabatic lapse rate, L is the latent heat of condensation, r_s is the saturation mixing ratio, and R_d is the ideal gas constant for dry air. From there, we calculate the Richardson number Ri:

$$\mathrm{Ri} = \frac{N_m^2}{\left(\frac{dU}{dz}\right)^2}, \qquad (2)$$

where the denominator is the vertical wind shear squared in terms of $U = (u, v)$ (Kirshbaum and Durran 2004; Geerts and Miao 2010). Note that Ri, N_m^2, and $(dU/dz)^2$ are subject to a 400-m moving average filter to reduce high-frequency noise.

We utilize a Ka band vertically pointing Micro Rain Radar (MRR) located at the PJ DOW site (Fig. 1) to visualize the overriding precipitation structures (Löffler-Mang et al. 1999; Aikins et al. 2016). MRR data were postprocessed following the technique of Maahn and Kollias (2012), to dealias Doppler velocity and enhance the use of MRR for solid precipitation

TABLE 1. Operations for Packer John (PJ) and Snowbank (SB) radars and the University of Wyoming King Air (UWKA) aircraft on 18 Jan 2017. Radar scan strategy includes 360° azimuthal or plan position indicator (PPI) scans and vertical cross sections or range–height indicator (RHI) scans upwind and downwind from the radar. The RHI scan along the UWKA flight track is highlighted in boldface. Both radars conducted Z_{DR} calibration scans at 89° elevation angle every 12 min, which is averaged over the entire observational period and applied to raw Z_{DR} values with uncertainty of ±0.2 dB.

	Operations
SB radar	PPIs at −1° to 70° elevation every 6 min with Δ1° between −1° and 9°, Δ2° between 11° and 17°, Δ3° between 20° and 35°, and Δ5° between 39° and 69°
PJ radar	RHIs at 51°/231° azimuth, 53°/233°, **55°/235**°, 57°/237°, 58°/238°, 59°/239° every 2–4 min
UWKA	Ten ~85-km-long, WSW–ENE–oriented transects (~17 min per transect) between 2000 and 2300 UTC flown in the opposite direction as the previous one at ~4.5 km MSL (15 kft; −8° and −10°C)

studies. MRR reflectivity and Doppler velocity were sampled at 100-m vertical resolution over 31 range gates, extending from the surface to 3 km AGL, and were averaged over 1-min intervals. The two lowest range gates yield unreliable data and were removed in postprocessing, and, thus, the MRR provides precipitation profiling from 0.2 to 3.0 km AGL (~2.3–5.1 km MSL).

Along with the MRR, a laser-optical particle size and velocity (PARSIVEL) disdrometer was located at the PJ DOW site (Fig. 1; Löffler-Mang and Joss 2000; Friedrich et al. 2016). The PARSIVEL samples the size and fall velocity of particles with diameters between 0.25 and 25 mm and fall velocities up to 22.4 m s^{-1}, providing full particle size distributions. For more information on PARSIVEL specifics and use in snow, see Battaglia et al. (2010). These snowfall metrics are used to compute a liquid equivalent snowfall rate using the methods of Brandes et al. (2007) and Aikins et al. (2016). Ice crystals that fall partially within the sampling range can result in an overestimation of the presence of small ice crystals. Therefore, ice crystals of $D < 1$ mm are removed from the analysis. PARSIVEL data sampled at 10-s intervals were then averaged over 1 min to match the temporal resolution of the MRR. We use PARSIVEL observations to validate snow falling from the KH waves aloft and, in concert with the MRR, to understand the snowfall composition.

3. Case overview

a. Synoptic setup

At 2100 UTC 18 January 2017, a broad region of surface low pressure extended across the eastern North Pacific from the northwest contiguous United States toward the Aleutian Islands of Alaska (Fig. 2). The system was beginning to occlude and a surface cold front was coincident with the coastline of Washington and Oregon. Simultaneously, high pressure existed over southeastern Idaho, Utah, and western Wyoming and Colorado. The location of the low and high pressures was ushering in pre-cold-frontal, warm, moist flow through northern California toward Idaho. As noted by Cann and Friedrich (2020), backward air particle trajectories suggested that 2100–2300 UTC was associated with a change in moisture pathway, i.e., a change in air mass. Atmospheric soundings launched at 2200 UTC 18 January and 0100 UTC 19 January indicated that winds above 5 km MSL shifted ~10° counterclockwise and the midtroposphere was warming via warm air advection as the 500-hPa trough approached. This synoptic-scale warm air advection was likely the cause of midtropospheric ascent that produced a precipitation shield spanning northern and central California, northern Nevada, eastern Oregon, and southwestern Idaho. Just prior to the onset of synoptic-scale ascent, when the moisture pathway and air mass were changing, is when the KH wave train passed over PJ mountain.

b. Sounding analysis

The atmospheric sounding launched at 2200 UTC captured the environmental conditions during the passage of KH waves (Fig. 3). From the surface to 6.5 km MSL, the atmosphere was near saturation (i.e., close T and T_d in Fig. 3a) with specific humidity (q) of 0.5–4.2 g kg^{-1} and maximum q at 3 km MSL (Fig. 3b). Above 6.5 km MSL was drier air with $q < 0.5$ g kg^{-1} indicating a cloud top height of 6.5 km MSL (Figs. 3a,b). Winds were primarily southerly below 2.5 km MSL, shifting to southwesterly up to 6.5 km MSL where they became increasingly westerly (Fig. 3c). Wind speed generally increased with height, sometimes rapidly over short distances, creating layers of strong wind shear. A strong shear layer ($5–10 \times 10^{-4}$ $s^{-2} \approx$ 22–32 m s^{-1} km^{-1}) existed between 6 and 6.6 km MSL, mainly driven by the increase in the zonal wind (Figs. 3c,d). Stability was moist-neutral above 3 km MSL and more stable

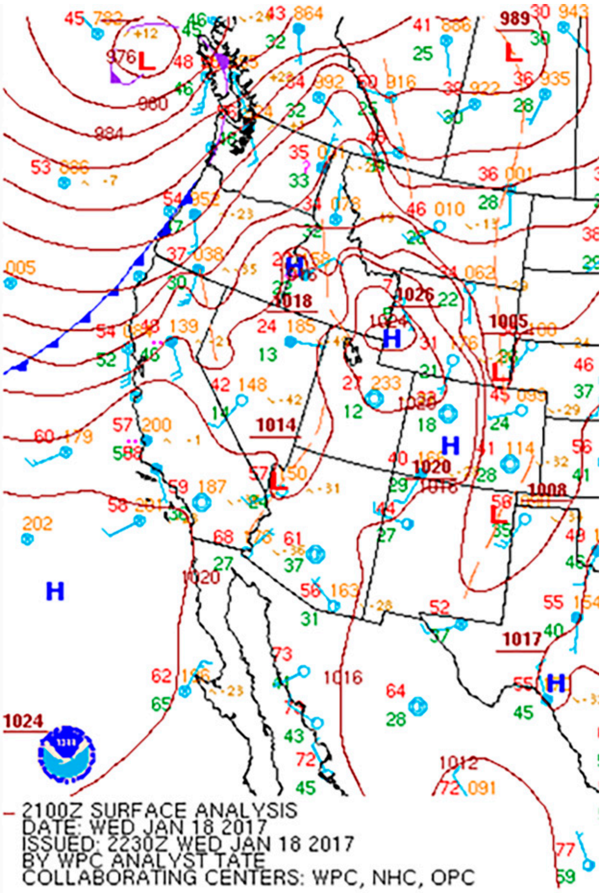

FIG. 2. Surface analysis across the western United States at 2100 UTC 18 Jan 2017 provided by the National Oceanic and Atmospheric Administration (NOAA) Weather Prediction Center (WPC). Station model consists of temperature (upper right; °F), dewpoint temperature (lower left; °F), wind direction and speed (small barb = 5 kt, large barb = 10 kt; 1 kt ≈ 0.51 m s^{-1}), coded station pressure (upper right; hPa), sky cover (within circle), and current weather observation (left). Isobars are indicated as solid brown lines. Location of high and low pressure systems and frontal systems are highlighted. Dashed orange lines indicate troughs. For more detailed descriptions, see https://www.wpc.ncep.noaa.gov/html/stationplot.shtml and https://www.wpc.ncep.noaa.gov/html/fntcodes2.shtml

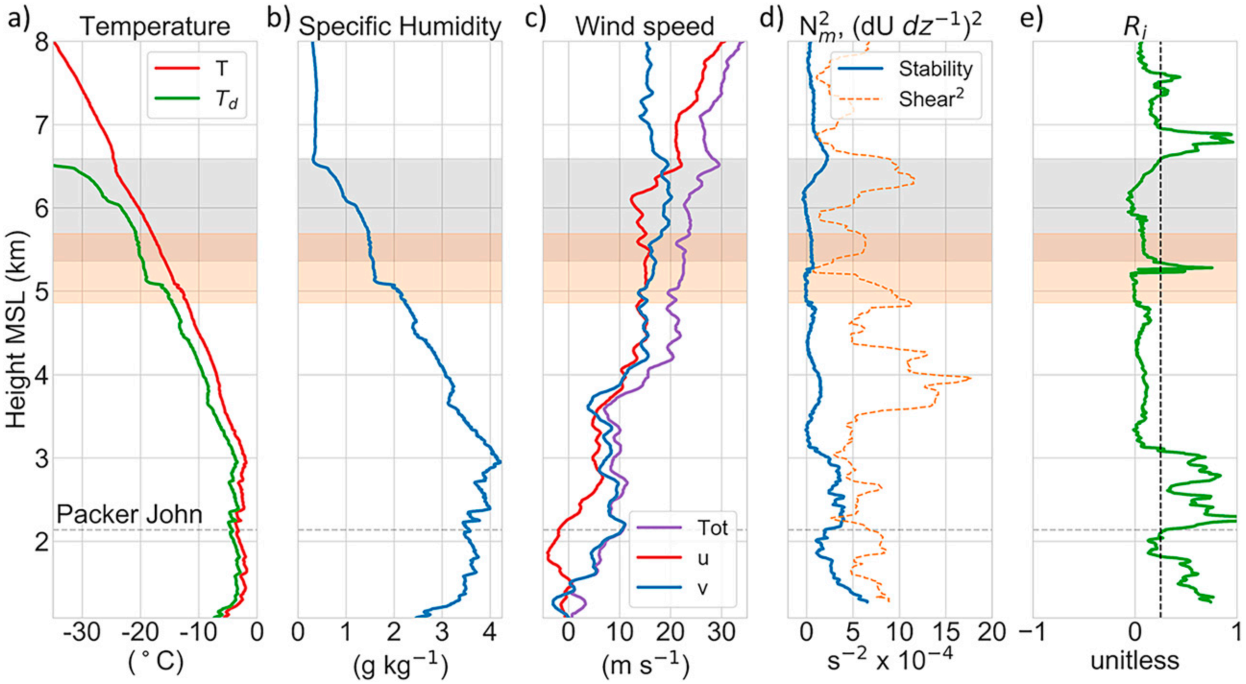

FIG. 3. Rawinsonde analysis from the sounding launched at 2200 UTC 18 Jan 2017 at location shown in Fig. 1 including (a) temperature and dewpoint temperature, (b) specific humidity, (c) total wind speed and zonal (u) and meridional (v) components, (d) moist stability and squared shear (shear^2), and (e) Ri. The gray shaded region is the layer of Ri < 0.25 near cloud top where KH waves are expected (5.4–6.6 km MSL). The orange shaded region is the DGZ (4.9–5.7 km MSL) with dark orange indicating the overlap between gray and orange. The altitude of Packer John Mountain is shown by gray dashed lines.

within the mountain valley below (Fig. 3d). The moist-neutral conditions allowed for Ri < 0.25, the critical threshold for KH wave formation, through much of the troposphere (Fig. 3e), even where shear was weak ($<3 \times 10^{-4}$ s^{-2}). Note that 300-m-deep layers of Ri < 0 existed where $N_m^2 < 0\,\mathrm{s}^{-2}$ between 4.9 and 5.2 km MSL and 5.9–6.2 km MSL indicating potential instability that can be released by rising parcels of saturated air. Potentially unstable layers of similar depth were observed by Geerts and Miao (2010) in a KH wave event. Cloud-top KH waves are expected within the 5.4–6.6 km MSL layer where Ri < 0.25 occurs at the ceiling of the near saturated layer (Fig. 3, gray shading). This KH wave layer, with $-16° < T < -24°$C, partially encompasses the DGZ (4.9–5.7 km MSL; Fig. 3, orange shading). Temperatures between −16° and −24°C favor the growth of plate-like particles, suggesting that observations of plates could be linked to ice formation from the KH waves (Bailey and Hallett 2009).

c. *DOW PPI analysis*

A cluster of five enhanced Z_e regions ($Z_e > 0$ dBZ_e) at 5 km MSL were advected from the southwest into the radar domain at 2100 UTC, ~1 h before the arrival of the deep synoptic cloud (Fig. 4). The Z_e regions progressed along the mean wind direction (220°) within the KH wave layer (5.4–6.6 km MSL). The regions were 15–50 km long and 5–20 km wide and exhibited axial ratios between 2 and 5 with the major axis oriented quasi-parallel to the mean wind direction. Regions 1–4 exhibited weaker Z_e (5–15 dBZ_e) along the leading edges and Z_e maxima (>25 dBZ_e) toward the rear.

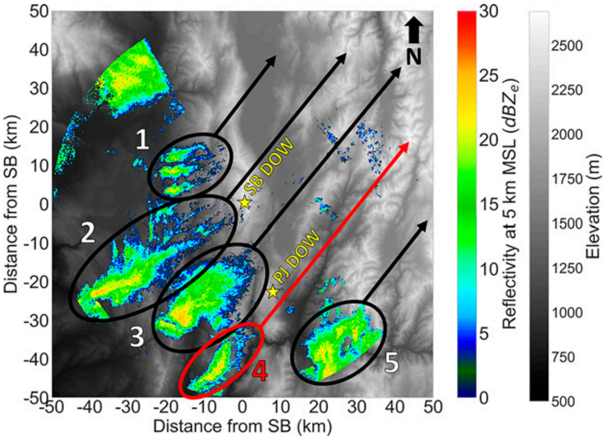

FIG. 4. Topographic map (gray shading) and Z_e at 5 km MSL (color shading) at 2123 UTC 18 Jan 2017 observed by the SB DOW. The red oval indicates the KH wave train that is the focal point of this study. Black ovals indicate regions speculated to be additional KH wave trains. Black and red arrows represent the trajectory of KH wave trains guided by southwesterly flow.

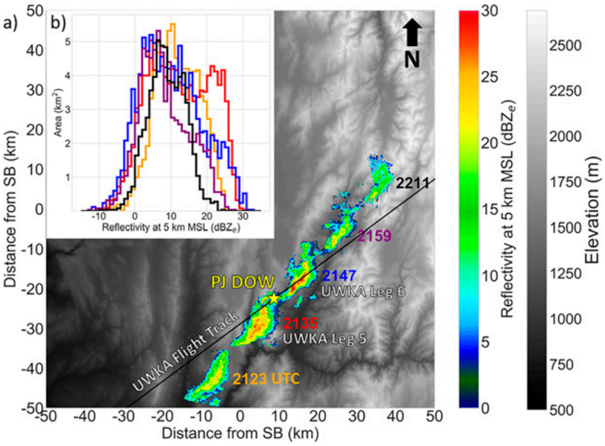

FIG. 5. (a) Topographic map (grayscale) with time series of DOW Z_e at 5 km MSL between 2123 and 2211 UTC (color coded) associated with region 4 in Fig. 4. UWKA flight track is overlaid; UWKA flight legs 5 and 6 match up with 2123 and 2147 UTC DOW Z_e, respectively. (b) Z_e distribution for each color-coded time step. The UWKA flight track is overlaid with the flight legs matching the time steps of the Z_e progression.

4. KH wave identification and progression

As region 4 moved through the radar domain (circle in Fig. 1) between 2123 and 2211 UTC, its size enlarged from 82 to 104 km^2 between 2123 and 2135 UTC and maximum Z_e increased from 25 to 30 dBZ_e at 5 km MSL (Fig. 5a). The area continuously decreased after 2135 UTC and Z_e diminished with <1 km^2 exceeding 20 dBZ_e by 2211 UTC (Fig. 5b). At 2135 UTC, region 4 began to pass over the PJ DOW and the UWKA flight track crossed the region for the first time (UWKA leg 5; Fig. 5a). WCR observations from leg 5 intersected the front edge of region 4 at about 2135 UTC, when DOW Z_e shows region 4 with a bimodal distribution (peaking at 5 and 22 dBZ_e) and the largest area (27 km^2) of $Z_e > 20$ dBZ_e (Fig. 5b, red line). WCR observations show a plume of $Z_e > 10$ dBZ_e between 4.5 and 5.5 km MSL directly above PJ (Fig. 6a), most likely contributing to the higher maxima of the bimodal distribution. Slightly above this region (5.5–6.5 km MSL) we first observed up- and downdraft couplets typically associated with KH waves (Grasmick and Geerts 2020), as shown in Fig. 6b. Within the KH wave region, cloud tops ranged from 6.5 to 6.8 km MSL (−25°C) and the highest Z_e (>15 dBZ_e) in leg 5 is observed just below the KH waves. Downwind of the KH waves (5–45 km northeast of PJ) were clouds with 6 km MSL tops at $T = -20°\mathrm{C}$ (Figs. 3, 6a). Shafts of higher Z_e downwind of PJ are most likely associated with cloud-top generating cells based on the dimensions and vertical velocity structure (Kumjian et al. 2014; Rauber et al. 2015; Keeler et al. 2017). Upwind of the KH waves, the cloud top descends to 4 km MSL (−8°C).

By 2147 UTC, the area of $Z_e > 0$ dBZ_e had decreased to 95 km^2 and the distribution had returned to a single mode peaking at 5 dBZ_e (blue line in Fig. 5b); the single mode continued through the remainder of DOW observations. The large area (27 km^2 at 2135 UTC) of $Z_e > 20$ dBZ_e had decreased to 16 km^2 by 2147 UTC, whereas the maximum Z_e of 32 dBZ_e was observed at this time (Fig. 5b). It is unclear why the Z_e region undergoes this temporary expansion and change in distribution. Leg 6 intersected the center of region 4 at 2147 UTC (8–20 km downwind of PJ; Figs. 6 c,d). Leg 6 Z_e and w show that cloud-top KH waves produced fluctus clouds (Figs. 6c,d). Fluctus are defined by the World Meteorological Organization as "a relatively short-lived wave formation, usually on the top surface of the cloud, in the form of curls or breaking waves (Kelvin–Helmholtz waves)." (WMO 2017). The wave breaking structure may indicate that the KH waves were beginning to dissipate as decreases in area and intensity of Z_e occurred thereafter (Fig. 5). DOW radar analysis at 2159 and 2211 UTC indicated that the area of $Z_e > 0$ dBZ_e first decreased to 71 km^2 and then 61 km^2 and the area of $Z_e > 20$ dBZ_e decreased to 5 km^2 and then to 1 km^2 (Fig. 5b, purple and black lines). Similarly, the max Z_e decreased to 27 and 24 dBZ_e at 2159 and 2211 UTC (Fig. 5b), respectively, and the $Z_e > 0$ dBZ_e echo top descended from 7 km MSL at 2147 UTC to 6.25 km MSL at 2211 UTC (not shown). Region 4 moved out of the radar domain before completely dissipating and was observed for a total of one hour and 18 min. Other studies have noted that KH wave lifetime is generally 1–2 h (e.g., Friedrich et al. 2008; Medina and Houze 2016), but can be longer, especially if internal circulations prolong the dynamical forcing (e.g., Petre and Verlinde 2004; Barnes et al. 2018). We now focus on zoomed-in portions of legs 5 and 6 to study the detailed KH wave kinematics and concurrent dual-polarization RHI scans from the PJ DOW to link cloud-top KH wave kinematics and the microphysical growth of ice.

5. KH wave kinematics and microphysical growth of ice

a. Wave kinematics

The structure of the KH wave train consisted of four to five w couplets of anterior subsidence and posterior lift during legs 5–6 extending over a distance of ~6–7.5 km resulting in a ~1.5 km wavelength (Fig. 7). Notably, the short wavelengths of the KH waves are too small to be resolved by operational weather model grid spacing (≥3 km) or even many higher-resolution modeling studies of KH waves (e.g., Mahalov et al. 2011; Trier et al. 2012; Conrick et al. 2018). The w couplets extended ~200 m into the DGZ (4.9–5.7 km MSL) during leg 5, while couplets 1 and 2 during leg 6 extended through the entirety of the DGZ. Maximum updraft speeds for each wave varied from 1.4 to 3.8 m s^{-1} (2.6 m s^{-1} average) during leg 5 and from 3.5 to 5.1 m s^{-1} (4.3 m s^{-1} average) during leg 6. The average maximum updraft speed during leg 6 was ~66% faster than during leg 5 and was fastest in the fluctus region that extended from 6 to 6.8 km MSL (Fig. 7b). The fluctus region was likely very turbulent as the up- and downdrafts were separated by ~100 m. Just beneath the fluctus, between 4.5 and 6 km MSL, the maximum updrafts were much weaker than within the fluctus (<1.5 m s^{-1}). These differences are important with respect to where the ice crystals form as updraft speed and particle size distribution dictate ice

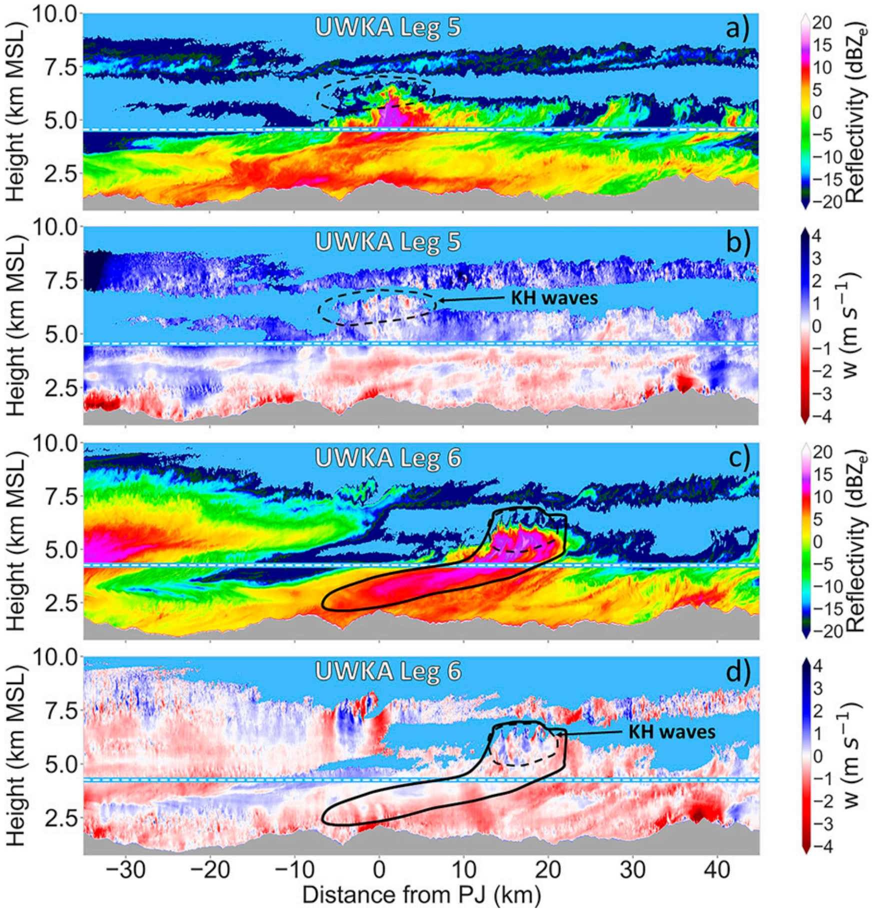

FIG. 6. UWKA WCR data with (a) Z_e during leg 5 (2127–2138 UTC) and (b) w during leg 5, (c) Z_e during leg 6 (2140–2157 UTC), and (d) w during leg 6. Updrafts are indicated in blue and downdrafts in red in (b) and (d). UWKA flight track is indicated by white dashed line. Dashed black lines indicate the KH wave region. Solid black outlined regions indicate the KH wave snow plume; data within the region are used for CFAD analysis. Sky blue areas indicate no data; gray areas indicate the underlying terrain.

supersaturation (Korolev and Mazin 2003) and certain ice crystals such as dendrites require supersaturation over both ice and water in addition to ambient temperatures in the DGZ (Bailey and Hallett 2009).

b. *Microphysical processes within the KH waves*

1) OBSERVATIONS DURING UWKA LEG 5 (2127–2138 UTC)

Based on the region of Z_e gradient, the weaker updrafts ($w < 1.5$ m s^{-1}) appear to be more important in facilitating production and growth of hydrometeors within the KH waves than the maximum upward motion isolated near cloud top (Fig. 8). The gradient from $Z_e \approx -20$ dBZ_e to $Z_e \approx 10$ dBZ_e designates the region of primary production/growth of hydrometeors where cloud-sized particles are converted to precipitation-sized ice crystals (black lines in Fig. 8). Note that this Z_e gradient does not occur at the top of the cloud where the maximum vertical velocities were observed (Fig. 7a), but instead within lower-altitude regions with >0.5 m s^{-1} updrafts (blue lines in Fig. 8). The strongest upward motion at cloud top may be unable to produce hydrometeors due to the overturning circulation of the KH waves entraining dry air and causing conditions to be less saturated than in the weaker updrafts located beneath the entrainment zone. Within these weaker updrafts were pockets of >1 m s^{-1} (dotted blue lines in Fig. 8) that spanned a few hundred meters in height and length (e.g., 5.9–6.2 km MSL in KH wave 3; 5.3–6 km MSL in KH wave 4). These updraft pockets likely provided supersaturated environments with SLW, favorable for the production of new ice crystals, increasing concentration, and growth in size of branched ice species, such as dendrites and sector plates, through deposition as well as the potential for riming (Majewski and French 2020; Rauber et al. 2019). Both an increase in particle concentration and size act to increase Z_e over this gradient region. Dual-polarization radar can provide more information on the specific ice species produced by the KH waves; however, we abstain from this analysis during leg

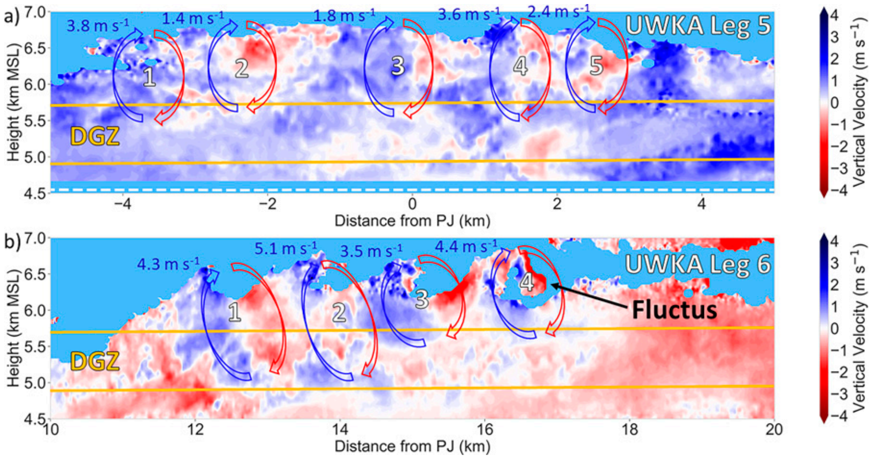

FIG. 7. Equal-area plots of w measured by the UWKA WCR during (a) leg 5 and (b) leg 6. Blue and red arrows highlight schematically up- and downdrafts of each KH wave (numbered). Blue numbers represent the maximum updraft speed in each wave. UWKA flight track is indicated by white dashed line in (a). Sky blue areas indicate no data (i.e., no cloud). The dendritic growth zone (DGZ) is shown between the orange lines (4.9–5.7 km MSL).

5 because the KH waves are positioned directly above the PJ DOW and in the cone of silence between the upwind and downwind RHI scans.

2) OBSERVATIONS DURING UWKA LEG 6 (2140–2157 UTC)

During UWKA leg 6, the KH waves moved 10–20 km downwind of PJ. The observations depict a more coherent structure of the w couplets, fluctus cloud top, and individual shafts of enhanced Z_e descending from the updrafts (Fig. 9a). Immediately upwind of each updraft and downwind of the subsequent downdraft from the next KH wave, regions of enhanced Z_e were lifted into the rear of the fluctus, rather than from ice generated in the fluctus region itself. In the center of each w couplet immediately upwind of the downdraft were local minima in Z_e. These Z_e maxima and minima were observed by the WCR Z_e between 6 and 6.5 km MSL (Fig. 9a). Note that we cannot observe the same detail in the DOW Z_e, a result of the coarser resolution with respect to the WCR (Fig. 9b). The main difference between the WCR and DOW Z_e is that the enhanced Z_e shafts beneath the updrafts merge to form a single snow plume of $Z_e > 20$ dBZ_e at ~4.6 km MSL, whereas the WCR Z_e remains in separate shafts. Note that we observe Z_e increasing from −20 dBZ_e to 10 dBZ_e as we did in leg 5 (Fig. 8), over depths as shallow as 200 m (Fig. 9a, gray boxes), compared to the region of Z_e gradient in leg 5 which ranged in depth from 0.5 to 1 km. Within and directly below these updrafts in the gray boxes, we observe WCR Z_e increase from 10 to 20 dBZ_e suggesting an

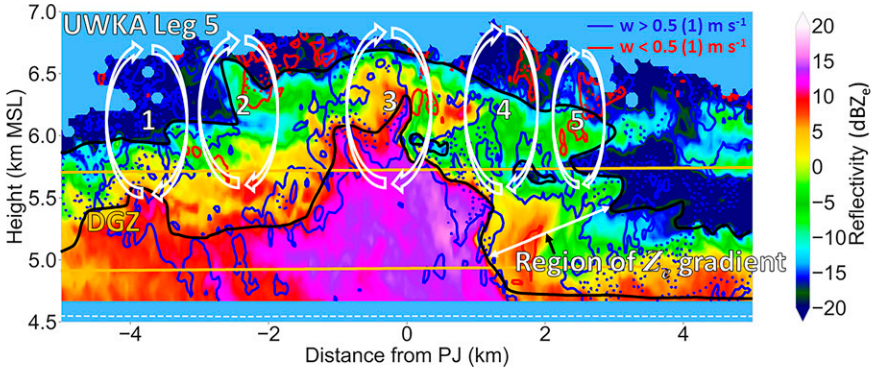

FIG. 8. As in Fig. 7a, but for Z_e (color-coded) observed during UWKA leg 5. Contours of w are at ±0.5 m s^{-1} (solid blue for positive and solid red for negative) and ±1.0 m s^{-1} (dotted blue for positive and dotted red for negative). The black lines roughly indicate the region of Z_e gradient from −20 to 10 dBZ_e. White arrows highlight schematically up- and downdrafts of each KH wave as in Fig. 7a (numbered). The dendritic growth zone (DGZ) is shown between the orange lines (4.9–5.7 km MSL).

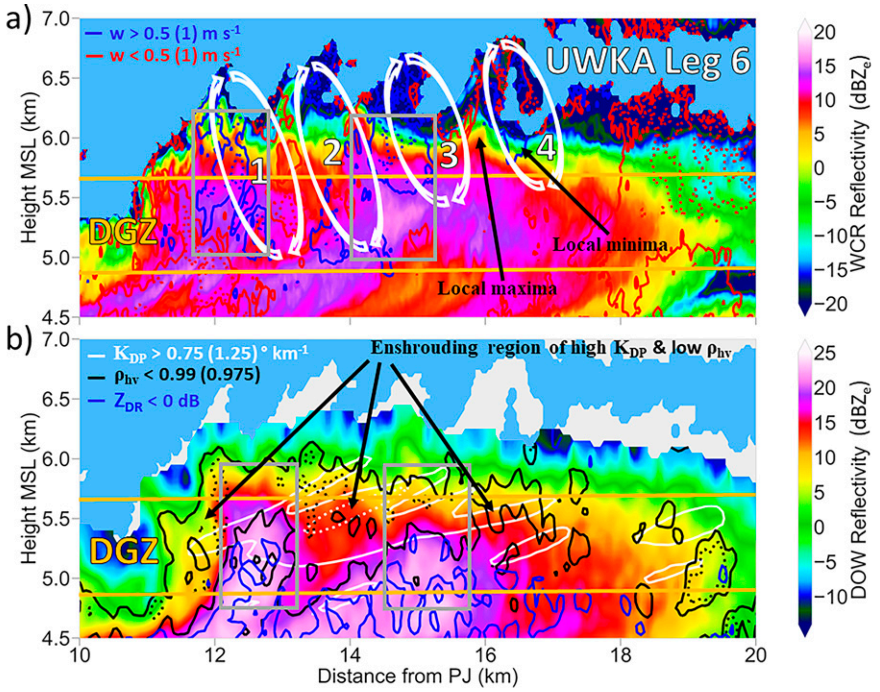

FIG. 9. (a) As in Fig. 8, but for UWKA leg 6. (b) Composite dual polarization measurements from the PJ DOW. In both panels, the following data are plotted: Z_e (color-coded), $K_{\mathrm{DP}} > 0.75° \mathrm{~km}^{-1}$ (solid white line), $K_{\mathrm{DP}} > 1.25° \mathrm{~km}^{-1}$ (dashed white line), $\rho_{\mathrm{hv}} < 0.99$ (solid black line), $\rho_{\mathrm{hv}} < 0.975$ (dashed black line), and $Z_{\mathrm{DR}} < 0$ (solid blue line). Sky blue indicates no data; white in (b) indicates cloud region from the WCR. The dendritic growth zone (DGZ) is shown between the orange lines (4.9–5.7 km MSL). Gray boxes indicate regions where updrafts are producing clear individual shafts of snow.

additional stage of secondary growth beyond the region of primary production/growth of precipitation-sized hydrometeors discussed previously. The use of DOW dual-polarization radar allows us to better understand the microphysical processes occurring within and below these updrafts.

The DOW RHI scans between 2142 and 2144 UTC show the entire KH wave snow plume as it extended down to the surface (Fig. 10a). The KH wave snow plume is loosely defined as the region where DOW $Z_e > 7$ dBZ_e between the surface and cloud top as outlined in Fig. 10. The plume was slanted with faster winds aloft pushing the clouds and precipitation farther downwind. The appearance of the snow plume decreasing in Z_e with decreasing altitude below 3.5 km MSL is due to the misalignment of the KH wave progression (220°) and the DOW RHI angle (235°). Simply put, the heaviest snow was falling elsewhere and only the edge of snow plume was intercepting PJ. Within and just beneath the KH wave train (Fig. 10, gray boxes) shows DOW Z_e increase from -5 dBZ_e to as high as 25 dBZ_e. As Z_e increases toward the surface, we observe Z_{DR} decrease from 3 dB to zero or slightly negative values. In this same region was $K_{\mathrm{DP}} > 0.75° \mathrm{~km}^{-1}$ with isolated areas of $K_{\mathrm{DP}} > 1.25° \mathrm{~km}^{-1}$ and $\rho_{\mathrm{hv}} < 0.99$. Positive Z_{DR}, high K_{DP}, and low ρ_{hv} together are strong indicators of an abundance of pristine planar ice crystals. Below the gray boxes and extending down to the surface, Z_e is large (15–25 dBZ_e) and Z_{DR} is near zero or slightly negative, indicating that the radar signals are dominated by large aggregates and heavily rimed particles. K_{DP} decreases with the transition from planar ice to aggregates below the gray box, but positive K_{DP} allows us to infer the presence of planar ice mixed with aggregates, especially where $K_{\mathrm{DP}} > 0.25° \mathrm{~km}^{-1}$ (Fig. 10c). These data depict a transition from pristine planar ice crystals with few or no aggregates near cloud top to decreasing concentrations of pristine planar crystals and increasing concentrations of aggregates as the snow plume approached the surface (Fig. 9b).

Returning attention to Fig. 9b, we have overlaid dual-polarization data in the KH wave region to better isolate the microphysical process. Enshrouding the $Z_e > 20$ dBZ_e region was an area of Z_e between ~0 and 20 dBZ_e, with $\rho_{\mathrm{hv}} < 0.99$ (Fig. 9b – black outline). The reduced ρ_{hv} and $K_{\mathrm{DP}} > 0.75° \mathrm{~km}^{-1}$ suggest that this enshrouding region was composed of fluttering pristine planar crystals which decreased ρ_{hv} and increased K_{DP}. Note that the depth of this enshrouding region is shallower (~0.5 km) within the gray boxes where the updrafts are located opposed to regions without updrafts where the enshrouding region is as deep as 1–1.5 km. Within the $Z_e > 20$ dBZ_e region, $\rho_{\mathrm{hv}} > 0.99$ and $Z_{\mathrm{DR}} \approx 0$ dB indicate an aggregate-dominated area. Therefore, we can conclude that the updrafts generate pristine planar ice crystals that are lifted

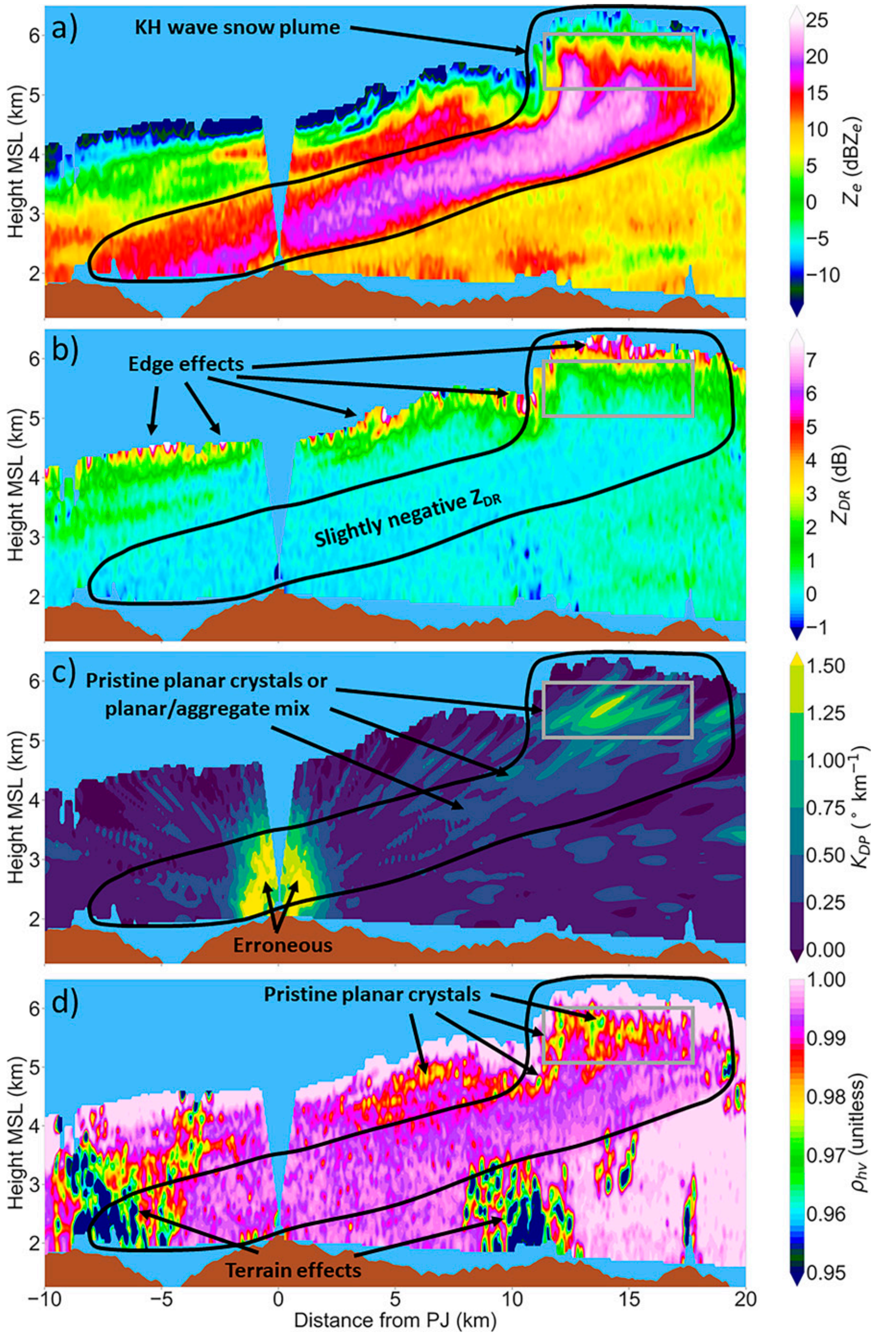

FIG. 10. PJ DOW RHIs at 2142 UTC (upwind) and 2144 UTC (downwind) for (a) Z_e, (b) Z_{DR}, (c) K_{DP}, and (d) ρ_{hv}. Black outlined regions indicate data used for CFAD analysis. Sky blue areas indicate no data; brown areas indicate the underlying terrain. The $Z_e < -5$ dBZ_e areas near the cloud top are a radar artifact, most likely related to nonuniform beam filling, which results in $Z_{\mathrm{DR}} > 4$ dB. Where Z_e is ≥ 0 dBZ_e, Z_{DR} maxed out around 3–4 dB, and Z_{DR} that exceed that maximum are likely erroneous. Gray boxes show the focus of microphysical changes that occurs just below the KH waves.

higher into the cloud by updraft speeds that exceed the fall speeds of the crystals and are then dispersed horizontally by turbulent winds. Ice crystals that are too heavy to be lifted out of the updrafts are instead suspended or recycled through the updraft where they continue to grow via deposition, aggregation, or riming, until sufficient size is reached that the fall speed exceeds the updraft speed and the ice begins to fall toward the surface. Thus, each updraft creates a shaft of

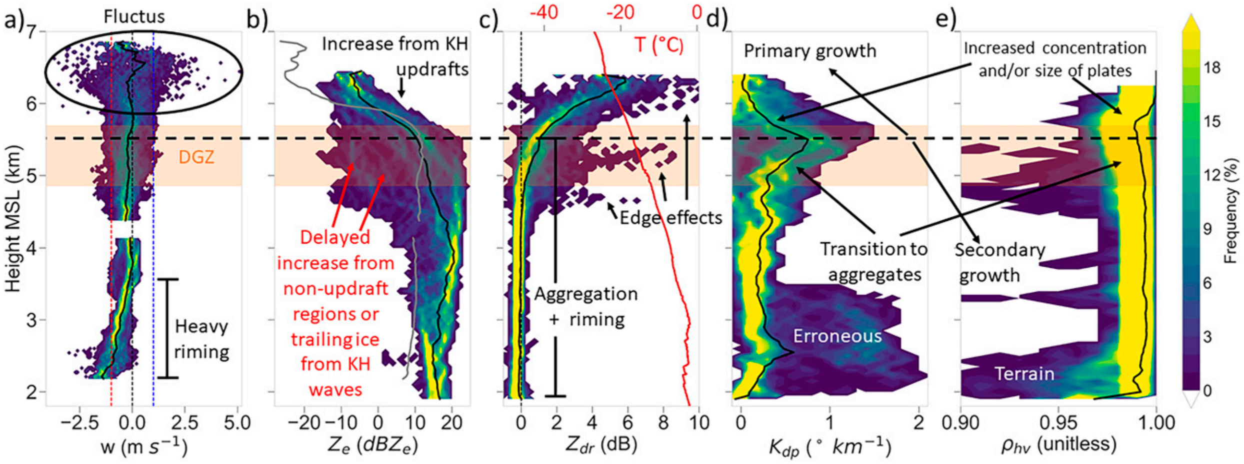

FIG. 11. CFADs for snow plume shown in Figs. 6c,d and 10: (a) UWKA leg 6 WCR w, (b) combined DOW and UWKA Z_e, (c) DOW Z_{DR} and temperature from the sounding, (d) DOW K_{DP}, and (e) DOW ρ_{hv}. Black lines show median value in (a)–(e). Red and blue dashed lines in (a) indicate -1 and 1 m s^{-1}, respectively. The gray line in (b) is the WCR Z_e median. The orange shading designates the DGZ (4.9–5.7 km MSL). The black dashed line separates the region of primary production/growth of hydrometeors aloft and the region of secondary growth beneath. Processes discussed in the text are highlighted.

enhanced Z_e comprised of rimed aggregates and planar ice crystals that form the KH wave snow plume.

The mechanism by which ice grows in the KH wave updraft appears to be similar conceptually, both kinematically and microphysically, to the cloud-top generating cells described by Kumjian et al. (2014, their Fig. 18) and the particle fountains described by Yuter and Houze (1995, their Fig. 15). A main difference is how the updrafts develop. Updrafts in thunderstorms or from cloud-top generating cells are produced from convective instability from radiative forcing and release of latent enthalpy and are organized by shear whereas updrafts from KH waves are produced and organized via shear instability (Yuter and Houze 1995; Kumjian et al. 2014; Keeler et al. 2017). The size and magnitude of the KH wave updrafts in our study are similar to that of cloud-top generating cells with ~1-km horizontal and vertical dimensions and ~1–2 m s^{-1} upward motion (e.g., Kumjian et al. 2014; Keeler et al. 2017). However, we only provide a single case study of cloud-top KH waves with 1.5-km wavelengths and studies have shown that KH wavelengths vary with the depth of the shear layer (e.g., Miles and Howard 1964; Turner 1973). Therefore, KH waves akin to those observed and modeled by Barnes et al. (2018) and Conrick et al. (2018) with ~5-km wavelengths may yield different kinematic and microphysical results at cloud-top than the KH waves presented herein. The microphysical processes appear to be more closely tied to the degree of supersaturation and ambient temperature, which are independent of the updraft source. For example, if the ambient temperature was −8°C near the KH wave updrafts, then needles would likely form which, when rimed, can reach 3 m s^{-1} fall velocity and may exit the updrafts much faster than dendrites or plates and potentially produce less snowfall. Without a larger sample of cloud-top KH waves, it remains unclear how the microphysical properties compare to cloud-top generating cells in a statistical sense in terms of ice concentrations and size distributions, and presence of SLW, as in Plummer et al. (2014), and, thus, more observations must be made.

3) CFAD ANALYSIS WITHIN THE KH SNOW PLUME

To further quantify and diagnose the microphysical processes occurring in the KH waves and in the cloud below, we created contoured frequency by altitude diagrams (CFADs; Yuter and Houze 1995). CFADs of w and dual-polarization data show the altitude of primary production/growth in size and concentration of pristine planar crystals beneath the fluctus (5.5–6.4 km MSL) and secondary growth processes of aggregation and riming between 5.5 km MSL and the surface (Fig. 11). Between 6 and 7 km MSL we observed $-4 < w < 5$ m s^{-1} (with 0 m s^{-1} median) within the fluctus of the KH waves (Fig. 11a). Between the surface and 6 km MSL, w rarely exceeded ±1 m s^{-1} except for small pockets of enhanced up- and downward motion, and strong downward motion ($w < -1$ m s^{-1}) near the surface (Fig. 11a). Within the KH wave updrafts and just above the DGZ (5.7–6.4 km MSL), increases in DOW Z_e (−5 to 10 dBZ_e) and WCR Z_e (−25 to 10 dBZ_e) were observed (Fig. 11b). With $-22° < T < -18$°C (Fig. 11c), we expect polycrystalline and sector plate shaped ice crystals to form (Bailey and Hallett 2009). Note that Z_{DR} within this region was affected by edge effects and is difficult to interpret (Fig. 11c). This branched platelike region is characterized by sharp increases in median K_{DP} (0–0.5° km^{-1} from 5.7 to 6.4 km MSL) and maximum values of 1.5° km^{-1} (Fig. 11c). Decreases in median ρ_{hv} from 1 to 0.99 over the same layer are observed (Fig. 11e). Whereas K_{DP} is sensitive to both particle size and concentration, ρ_{hv} in a region of planar ice crystals is sensitive only to the size/shape and orientation. With no preferred azimuthal orientation, fluttering plates of larger size and inherently different shape, or nonplanar polycrystalline plates with no preferred direction of

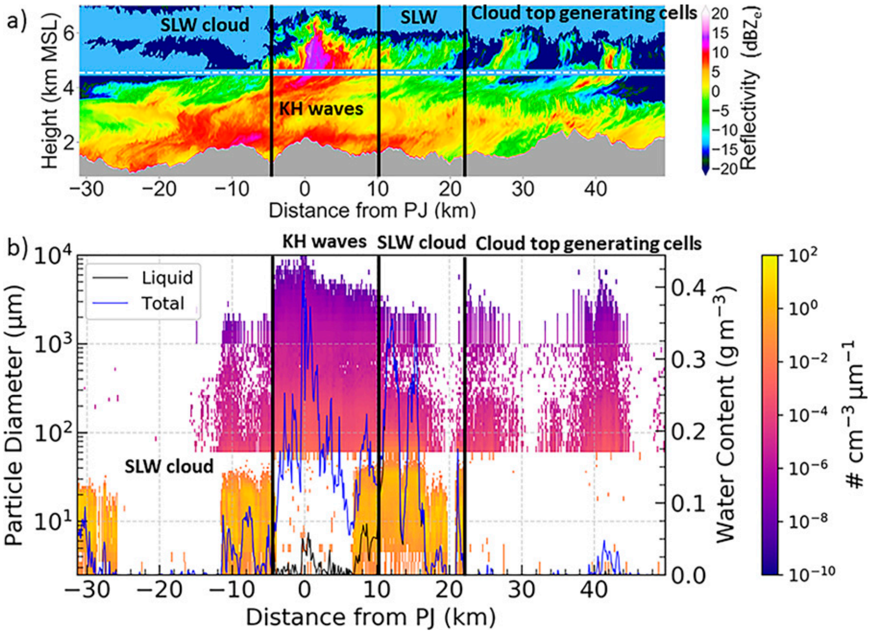

FIG. 12. Observations from UWKA leg 5: (a) WCR Z_e and (b) particle size distribution (color-coded) comprising CDP, 2D-S, and 2D-P, and Nevzorov liquid water content (black line) and total water content (blue line). The discontinuity in particle concentration from 50- to 75-μm diameter in (b) is the result of the lower detection limit of the 2D-S compared to the CDP.

branch growth, are the cause of decreased ρ_{hv} and likely much of the K_{DP} increase as altitude decreases (e.g., Kumjian 2013a, and references therein). Therefore, while both increases in particle concentration and size were occurring, we can designate the altitude range where median ρ_{hv} decreases with decreasing altitude as the region where the branched platelike ice crystals were increasing in size (5.6–6.2 km MSL; Fig. 11e).

Within the DGZ (4.9–5.7 km MSL), median K_{DP} continued to increase to a maximum of 0.8° km^{-1} at 5.5 km MSL before continuously decreasing toward the surface (Fig. 11d). This maximum turning point in K_{DP} designates the transition from primary growth of pristine ice crystals via deposition as the dominant microphysical mechanism to secondary growth via aggregation and riming. The increase of median K_{DP} within the DGZ suggests continued growth in size and/or concentration of pristine ice crystals, including dendrites if sufficient supersaturation was attained (Bailey and Hallett 2009; Kumjian 2013a). A maximum in pristine crystal concentration was likely collocated with the maximum median K_{DP} of 0.8° km^{-1} at 5.5 km MSL within the upper DGZ. In the lower portion of the DGZ (4.9–5.5 km) and into the top of the secondary growth region, median K_{DP} decreased to 0.3° km^{-1} and ρ_{hv} increased to about 1 (Figs. 11d,e). These changes indicate a decrease in concentration of pristine ice crystal due to aggregation and resulting in progressively more aggregates and fewer pristine ice crystals as the snow falls toward the surface.

From 5.5 km MSL to the surface, aggregation likely became gradually more efficient as temperature increases caused higher probability of a quasi-liquid layer on the ice crystal surface, encouraging collection (Hosler and Hallgren 1960; Ewing 2004; Bartels-Rausch et al. 2014; Constantin et al. 2018; Zeng and Li 2019). Growth via riming is also suggested, especially below 3.5 km MSL, indicated by the increase in fall-speed-corrected median downward velocity from 0 to -1.5 m s^{-1} (Fig. 11a) and decrease of median Z_{DR} to slightly negative values (Fig. 11c). The increase in downward velocity is probably due to densely rimed dendrites with fall speeds of 1–2 m s^{-1} and fractured ice from the aggregation and riming processes which likely formed graupel with fall speeds $>$ 2 m s^{-1} (Barthazy and Schefold 2006; Schrom and Kumjian 2016; Bringi et al. 2017). Riming was likely maximized below 3.5 km MSL where moisture content was largest ($>$3.5 g kg^{-1}), $T >$ -5°C, and SLW present (Fig. 3). To better understand how the snow falling from the KH waves continued to grow at the expense of the underlying SLW cloud, we utilize in situ cloud and precipitation observations from the in situ UWKA and surface observations.

6. In situ cloud and surface observations

a. *Observations during UWKA leg 5 (2127–2138 UTC)*

The in situ cloud probe data at ~4.25 km MSL show that the snow plume associated with the KH waves ($-5 < x <$ 8 km of PJ) was mostly devoid of liquid cloud droplets and consisted of increased concentrations of ice-phase particles with diameters (D) $>$ ~50 μm whereas clouds upwind and downwind were composed entirely of SLW cloud- and drizzle-sized drops (Fig. 12). During leg 5, we observed cloud structures 22–49 km downwind of PJ, that likely included

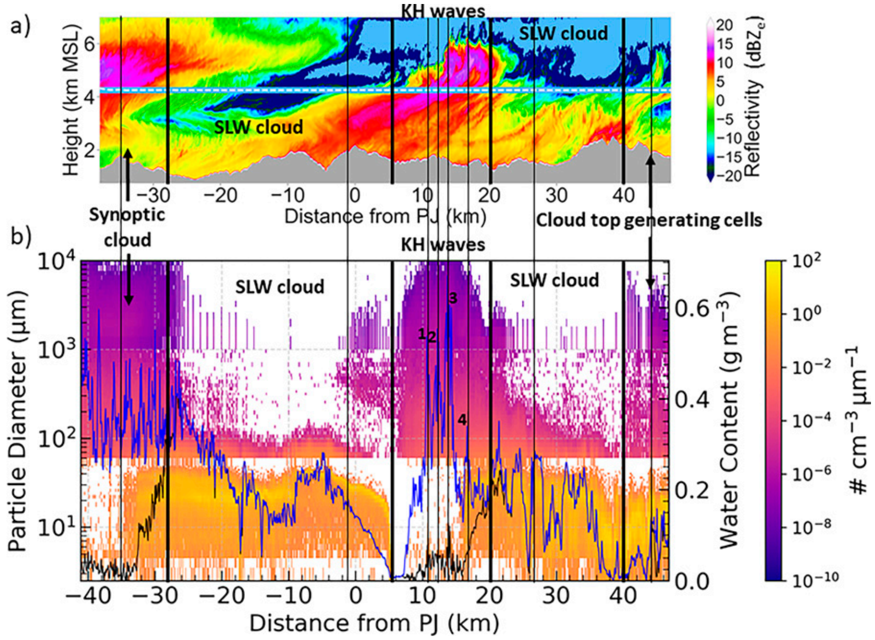

FIG. 13. As in Fig. 12, but for UWKA leg 6. Thin black lines show the locations of 2D-S images in Fig. 14. TWC spikes from the four KH waves labeled in Fig. 9a are labeled 1–4.

cloud-top generating cells, which produced descending shafts of ice particles with $D < 4$ mm, TWC < 0.05 g m^{-3} and roughly no LWC (Fig. 12b). Clouds 10–22 km downwind of PJ consisted mainly of cloud- and drizzle-sized particles ($D < 0.3$ mm) though some particles up to 2 mm existed, and water content was entirely in the liquid phase with LWC up to 0.3–0.4 g m^{-3} (Fig. 12b). Within the KH wave region ($-5 < x < 10$ km), clouds were mostly glaciated with $0.05 <$ TWC < 0.42 g m^{-3} and LWC < 0.1 g m^{-3}. KH wave snow plume particle size distributions show the presence of ice crystals with $0.1 < D < 10$ mm. This diameter range entails a possible mixture of aggregates ($D > 1$ mm), pristine ice crystals ($D \leq 1$ mm), supercooled drizzle ($D < 0.5$ mm), and very few cloud-sized particles in the CDP sampling range ($D < 50$ μm). These size distribution data suggest that most of the SLW has either evaporated and deposited on falling ice or has been depleted through riming (Fig. 12b). Residual LWC < 0.1 g m^{-3} suggests these processes are still occurring at this altitude.

b. Observations during UWKA leg 6 (2140–2157 UTC)

Leg 6 presents a similar story, except with higher TWC and larger ice crystals (Fig. 13). The cloud-top generating cells are now 40–50 km downwind of PJ and show pristine ice crystals $D \approx 0.5$–1 mm and relatively very few SLW droplets or drizzle (Fig. 14). The obscure structure of the ice crystals appear to be from heavy riming. The SLW cloud region extends 20–40 km downwind of PJ and consisted of an abundance of cloud- and drizzle-sized particles with $D < 0.5$ mm and LWC < 3 g m^{-3} and relatively few ice crystals (Figs. 13b, 14). The KH wave snow plume region contained TWC of 0.3–0.65 g m^{-3} and LWC < 0.1 g m^{-3}, notably higher TWC compared to the same region during leg 5 (Figs. 12b, 13b). The four spikes in TWC appear to be from snow descending from KH waves 1–4 in Fig. 9a and are labeled as such (Figs. 13b, 14). Notably, the largest TWC observed during leg 6 occurs from KH wave 3 (0.63 g m^{-3}) and not within the synoptic cloud (max TWC = 0.6 g m^{-3}) which cloud tops extend ~3 km higher than the KH waves. The leading edge of the KH wave snow plume (KH wave 4) is marked by a reduction of LWC from 0.2 g m^{-3} at 20 km to ~0 g m^{-3} at 16 km and a decrease in particle concentration from 7 cm^{-3} at 20 km to <1 cm^{-3} at 16 km, TWC remains consistent around 0.2 g m^{-3} with a shift toward larger sizes on the tail of the ice size distribution (Fig. 13b). KH waves 1–4 show various branched ice species which appear to include polycrystalline plates, sector plates, and dendrites mixed with varying amounts of smaller ice splinters, and supercooled cloud- and drizzle-sized droplets (Fig. 14). Ice smaller than the channel height of 1.28 mm are single planar or polycrystalline ice crystals and various aggregates of these particles can be observed as ice that extends beyond the height or along the width of the images. These data suggest that the small ($D < 50$ μm) SLW cloud droplets were continuously being rimed onto ice crystals from the KH waves with nonzero LWC < 0.1 g m^{-3} throughout the KH wave region and many of the ice crystals appear to be rimed. As we pass out of the KH waves from 5 to −5 km there is a transition back to a SLW cloud with LWC increasing from ~0 g m^{-3} at 5 km to 0.2 g m^{-3} at −5 km, and droplet D increasing from 5 to 40 μm. The particle concentration was consistently 7–10 cm^{-3} over this range, suggesting that ice crystals trailing from the KH waves are consuming most of the SLW cloud droplets within the wave region, but outside of the region, as concentration of ice particles and any subsequent riming slowly decreases, liquid water droplets are once

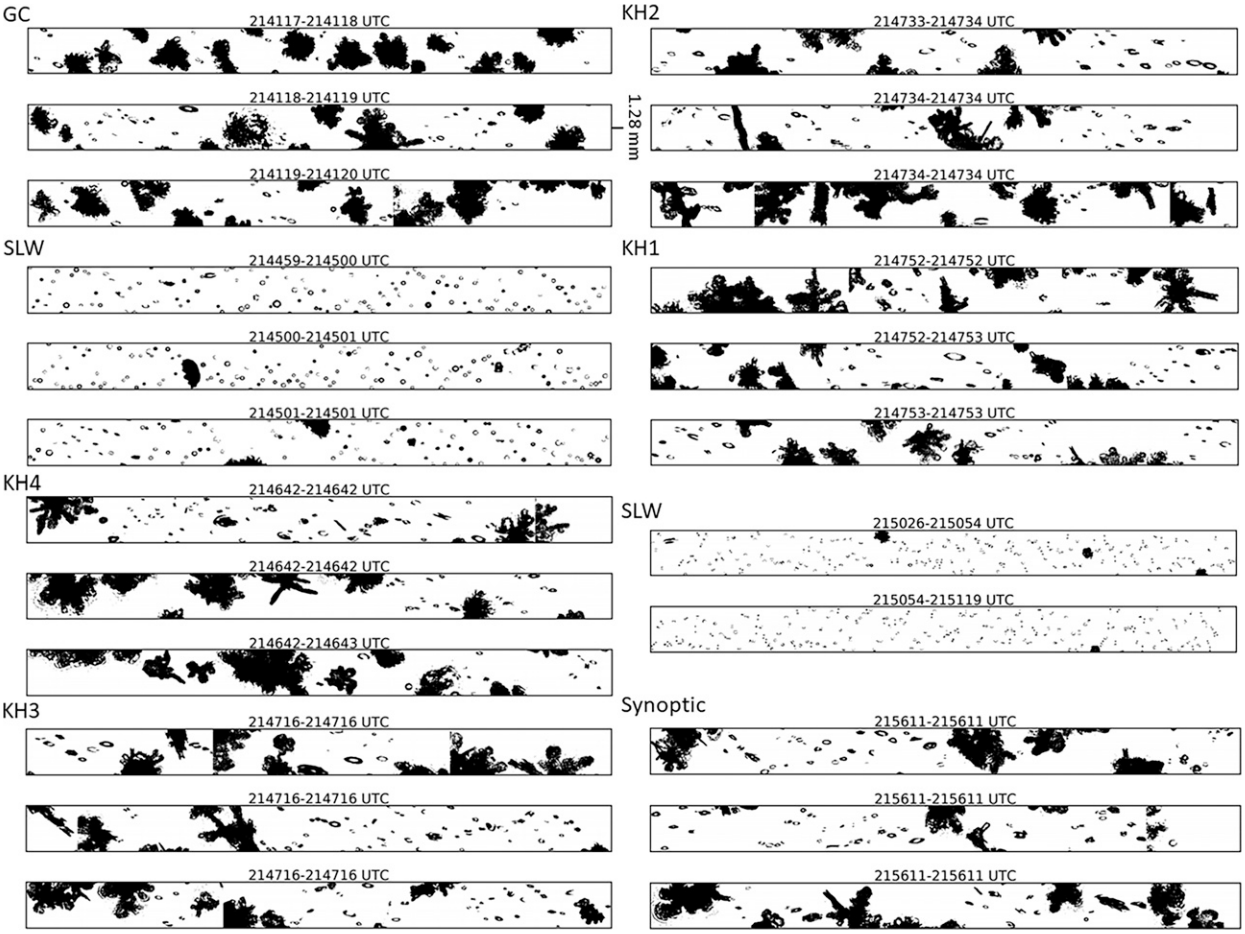

FIG. 14. Particle imagery from the 2D-S on board the UWKA at ~4.25 km MSL within the KH wave snow plume at the locations shown by thin black lines in Fig. 13. GC is cloud-top generating cells; SLW is supercooled liquid water clouds; KH1–4 are for KH waves labeled in Fig. 13b near their peak TWC. The height of the channel is 1.28 mm. Times above images correspond to the times of observation.

again able to grow through condensation and achieve sizes of ~40 μm and LWC in excess of 0.2 g m^{-3}.

Between 28 km upwind and 5 km downwind of PJ, a SLW cloud consisted of particles mainly $D < 0.1$ mm and LWC ranges between ~0 g m^{-3} near the KH wave snow plume to 0.5 g m^{-3} near the leading edge of the deep synoptic cloud (Figs. 13a,b, 14). The synoptic cloud system was generating TWC in the same magnitude range as the KH waves (0.3–0.6 g m^{-3}) and similar LWC < 1 g m^{-3}. These TWC and LWC data suggest that the KH wave region is just as effective in converting LWC to snow as the ~10 km MSL deep synoptic cloud (28–40 km upwind of PJ). Further, snow crystal size distributions ($D > 1$ mm) also appear similar within the KH snow plume and synoptic cloud, with particles reaching 10 mm in both environments (Figs. 13b, 14). As snow fell to the surface they may have continued to aggregate and rime causing changes in particle size and number concentration.

c. *Surface disdrometer and MRR*

Figure 15 depicts the MRR vertical reflectivity profile and surface snowfall characteristics associated with KH wave snow plume, the cloud-top generated cells, SLW clouds, and the synoptic cloud as they passed over the PJ DOW site. Note that the MRR minimum detectable signal is 0 dBZ_e and only extends ~3 km AGL and may not capture the entire depth of the precipitating system. In the cloud-top generating cell region (2100–2126 UTC), Z_e increased from 0 dBZ_e at ~4.5 km MSL to 17 dBZ_e at the surface (Fig. 15a). Low particle concentration (average: 35 m^{-3}) of relatively large size (average: 2.3 mm) and very few smaller particles ($D < 2$ mm) falling at an average of 2.7 m s^{-1} with considerable variance (Figs. 15b–d). These fall speeds suggest that ice crystals were heavily rimed (e.g., Schrom and Kumjian 2016; Bringi et al. 2017), but the ice does not amount to a large liquid-equivalent snowfall rate (hereafter LESnow; average 0.2: mm h^{-1}) due to low concentration of falling particles (Fig. 15e).

Between 2126–2144 UTC and 2157–2217 UTC echo tops descended to 3–4 km MSL during the period of SLW clouds (Fig. 15). These two periods exhibited similar average particle concentrations (312–399 m^{-3}), average mass-weighted diameters (2–2.7 mm), average fall velocities (1.8–1.9 m s^{-2}), and LESnow (0.5–0.7 mm h^{-1}). The snowfall rates were higher

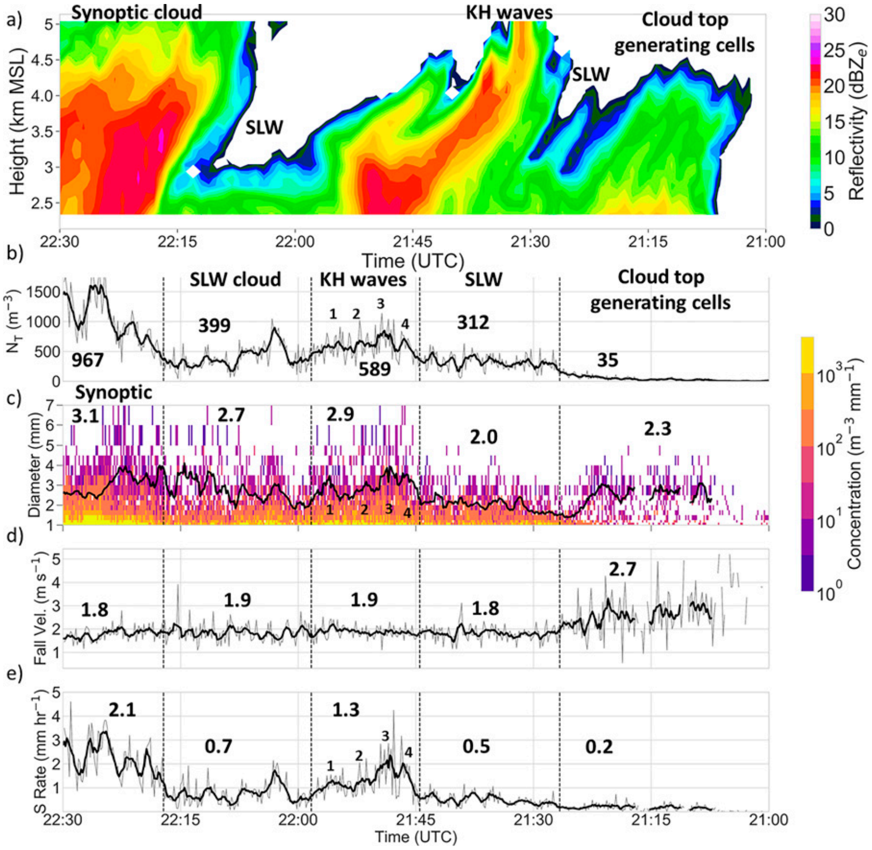

FIG. 15. (a) MRR Z_e, (b) PARSIVEL total particle concentration (N_T), (c) normalized particle size distribution (color coded) and mean mass-weighted particle diameter (black line), (d) mean particle fall velocity, and (e) liquid equivalent snowfall rate. Gray lines in (b), (d), and (e) show 10-s PARSIVEL data; black lines show 1-min moving average. PARSIVEL data have been shifted by 100 s to account for the time required for particles to fall between the lowest MRR range gate (200 m AGL) and the surface based on the observed fall speed at the surface of ~2 m s^{-1}. Vertical dashed lines separate the dominant precipitation processes and mean values within each segment are shown in (b)–(e). The individual KH waves from Figs. 9a and 13b are labeled 1–4. Note that time increases from right to left to match the perspective of Figs. 12 and 13.

from the SLW clouds than the cloud top generating cells, driven by an abundance of particles of $D < 2$ mm.

Between 2144 and 2157 UTC, the KH wave snow plume moved over PJ (Fig. 15a). The plume at 5 km MSL was advected over PJ as early as 2130 UTC and the snow took ~15 min to reach the surface. The individual KH waves labeled in Figs. 9a and 13b are labeled similarly here as 1–4 (Figs. 15b,e). The average particle concentration was 589 m^{-3}, which is 190–277 m^{-3} more than the SLW clouds. The particle concentration peaked during the passage of KH wave 3 at 1138 m^{-3}. The passage of each KH wave aloft can be observed at the surface in the 1-min moving averages (black lines in Fig. 15). Mean mass-weighted particle diameter increased from 2 mm up to 4 mm in KH wave 3. Similarly, the average LESnow during the KH waves was 1.3 mm h^{-1}, more than twice the LESnow of the SLW clouds and peaking at 4.2 mm h^{-1} during KH wave 3. The higher LESnow can be attributed to both larger aggregates (D as high as 10 mm were observed) and larger particle concentrations throughout the size spectrum.

After 2217 UTC, the synoptic cloud system passed over PJ (Fig. 15a). Particle concentrations during the synoptic cloud averaged 967 m^{-3} with a mean mass-weighted diameter of 3.1 mm and mean fall velocities of 1.8 m s^{-1} (Figs. 15b–d). The highest LESnow was observed at this time (4.6 mm h^{-1}) with an average of 2.1 mm h^{-1} (Fig. 15e). Note that the second highest 10-s LESnow was observed during KH wave 3. Given similar mean mass-weighted diameters of snow in the KH waves snow plume and synoptic cloud, the higher average LESnow in the synoptic cloud were driven by higher particle concentrations (max 2054 m^{-3}). However, TWC and particle size distributions at ~4.25 km MSL were observed to be similar in the KH snow plume and synoptic cloud (Fig. 13b). One possible explanation for the higher surface particle concentrations and LESnow from the synoptic cloud is the misalignment of the KH wave progression and the DOW RHI

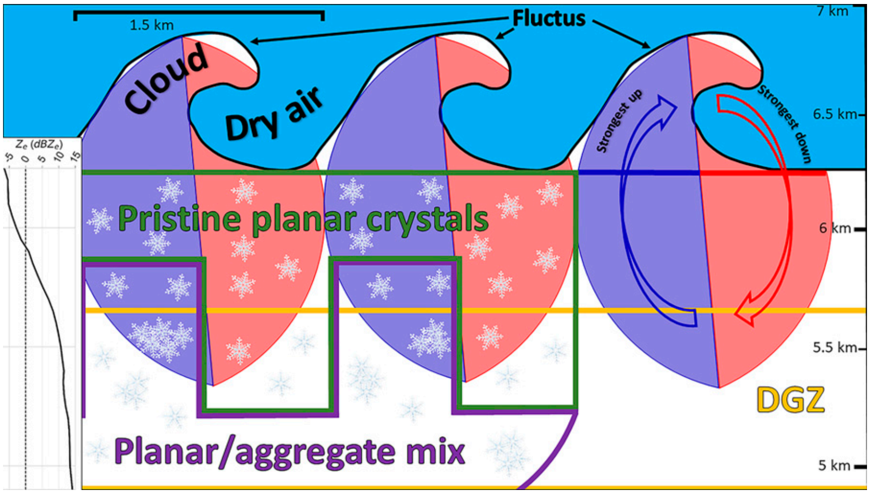

FIG. 16. Conceptual model describing the kinematic and microphysical processes in cloud-top KH waves near the DGZ as derived from this study. Blue and red ovals represent up- and downdrafts of 0.5–1.5 m s^{-1}, respectively, with the strongest vertical velocities in the fluctus region. Cloud and dry air are entrained within the fluctus region forming wave breaking cloud tops. The DGZ is shown between the orange lines. Generation and growth of pristine planar ice crystals is shown within the green-lined region. The transition to aggregation and accretion is shown in the purple-lined region, which together with the green region comprise the snow plume. The pristine planar crystal region transitions to the planar–aggregate mix region over thinner depths within the 0.5–1.5 m s^{-1} updrafts. The median Z_e by altitude is shown on the left side. Altitudes are MSL.

angle as shown by the apparent decrease in Z_e with altitude (Figs. 10a, 13a). This effect is evidenced by the lower LESnow in KH waves 1 and 2 compared to their relatively large TWC aloft, and means the heaviest snow sampled aloft fell elsewhere in the mountains (Figs. 13b, 15e).

7. Conclusions

This study presents one of the first observations of cloud-top KH waves that generated pristine ice crystals and a snow plume that extended to the surface. We observed a KH wave train advect through the Payette Mountains of Idaho, intensify, wave-break producing fluctus cloud features, and begin to weaken as it left the region. The main conclusions from this analysis are summarized schematically in Fig. 16 and below:

- Cloud-top KH waves with 1.5-km average wavelengths and 1.5-km-deep updraft and downdraft couplets and positioned within and above the DGZ were observed to produce snowfall that made it to the ground with four distinct peaks in snowfall intensity associated with the four KH waves aloft.
- Updrafts/downdrafts of ~750-m width and ~1.5-km depth up to 5 m s^{-1} were observed and the fastest up and downdrafts occurred in the fluctus. However, updraft speeds of 0.5–1.5 m s^{-1} beneath the fluctus were associated with the growth of pristine planar ice crystals and were identified across regions of WCR Z_e gradients from −20 to 10 dBZ_e over depths ranging from 200 to 1000 m, likely tied to updraft strength, size, and location. Growth of hydrometeors in cloud-top KH waves thus differs from within a precipitating layer where growth was observed in the KH wave crest (Houser and Bluestein 2011; Barnes et al. 2018). Cloud-top KH waves behave kinematically and microphysically similar to cloud-top generating cells where updraft were enshrouded with high concentrations of pristine planar ice particles exhibiting $K_{\mathrm{DP}} > 0.75°\ \mathrm{km}^{-1}$ and $\rho_{\mathrm{hv}} < 0.99$. Within and beneath the updrafts, growth continued by aggregation and riming.
- Snow descending from the cloud-top KH waves were efficient in glaciating the underlying SLW cloud, reducing average LWC from 0.25 to 0.04 g m^{-3}, similar to what was observed in the synoptic cloud. The largest TWC at ~4.25 km MSL was observed in the KH wave snow plume and not from the synoptic cloud.
- Average liquid equivalent snowfall rates at the surface were shown to increase twofold from 0.6 mm h^{-1} average during the SLW clouds to 1.3 mm h^{-1} during the passage of KH waves, due to increased particle sizes and concentrations.

Cloud-top KH waves near the DGZ can have substantial impacts on microphysical processes within the underlying clouds and surface precipitation rates due to the production of aggregation-efficient planar ice species. More observations are required to understand the frequency of cloud-top KH waves that produce snowfall, determine their ability to generate snowfall when located away from the DGZ, and provide a robust statistical analysis of cloud-top KH wave microphysical properties.

Acknowledgments. This research was supported under NSF Grant AGS-1546963 and AGS-2015829 and by the Idaho Power Company. We also acknowledge researchers and students from NCAR, University of Wyoming, University of Illinois at Urbana–Champaign, University of Colorado Boulder, and Center for Severe Weather Research for assistance with data collection and processing. Thank you to Josh Aikins. We also thank two anonymous reviewers for their comments that improved the quality of this manuscript.

Data availability statement. All data herein are publicly available from the Earth Observing Lab (EOL) data archive (https://data.eol.ucar.edu/master_lists/generated/snowie/).

REFERENCES

Aikins, J., K. Friedrich, B. Geerts, and B. Pokharel, 2016: Role of a cross-barrier jet and turbulence on winter orographic snowfall. *Mon. Wea. Rev.* **144**, 3277–3300, https://doi.org/10.1175/MWR-D-16-0025.1.

Andrić, J., M. R. Kumjian, D. S. Zrnić, J. M. Straka, and V. M. Melnikov, 2013: Polarimetric signatures above the melting layer in winter storms: An observational and modeling study. *J. Appl. Meteor. Climatol.*, **52**, 682–700, https://doi.org/10.1175/JAMC-D-12-028.1.

Atlas, D., J. I. Metcalf, J. H. Richter, and E. E. Gossard, 1970: The birth of "CAT" and microscale turbulence. *J. Atmos. Sci.*, **27**, 903–913, https://doi.org/10.1175/1520-0469(1970)027<0903:TBOAMT>2.0.CO;2.

Bailey, M. P., and J. Hallett, 2009: A comprehensive habit diagram for atmospheric ice crystals: Confirmation from the laboratory, AIRS II, and other field studies. *J. Atmos. Sci.*, **66**, 2888–2899, https://doi.org/10.1175/2009JAS2883.1.

Barnes, H. C., J. P. Zagrodnik, L. A. McMurdie, A. K. Rowe, and R. A. Houze, 2018: Kelvin–Helmholtz waves in precipitating midlatitude cyclones. *J. Atmos. Sci.*, **75**, 2763–2785, https://doi.org/10.1175/JAS-D-17-0365.1.

Bartels-Rausch, T., and Coauthors, 2014: A review of Air–Ice Chemical and Physical Interactions (AICI): Liquids, quasi-liquids, and solids in snow. *Atmos. Chem. Phys.*, **14**, 1587–1633, https://doi.org/10.5194/acp-14-1587-2014.

Barthazy, E., and R. Schefold, 2006: The fall velocity of graupel and of snowflakes of different riming degree and crystal types. *Atmos. Res.*, **82**, 391–398, https://doi.org/10.1016/j.atmosres.2005.12.009.

Battaglia, A., E. Rustemeier, A. Tokay, U. Blahak, and C. Simmer, 2010: PARSIVEL snow observations: A critical assessment. *J. Atmos. Oceanic Technol.*, **27**, 333–334, https://doi.org/10.1175/2009JTECHA1332.1.

Baumgardner, D., and Coauthors, 2017: Cloud ice properties: In situ measurement challenges. *Ice Formation and Evolution in Clouds and Precipitation: Measurement and Modeling Challenges, Meteor. Monogr.*, No. 58, Amer. Meteor. Soc., https://doi.org/10.1175/AMSMONOGRAPHS-D-16-0011.1.

Bechini, R., L. Baldini, and V. Chandrasekar, 2013: Polarimetric radar observations in the ice region of precipitating clouds at C-band and X-band radar frequencies. *J. Appl. Meteor. Climatol.*, **52**, 1147–1169, https://doi.org/10.1175/JAMC-D-12-055.1.

Brandes, E. A., K. Ikeda, G. Zhang, M. Schönhuber, and R. M. Rasmussen, 2007: A statistical and physical description of hydrometeor distributions in Colorado snowstorms using a video disdrometer. *J. Appl. Meteor. Climatol.*, **46**, 634–650, https://doi.org/10.1175/JAM2489.1.

Bringi, V. N., P. C. Kennedy, G. Huang, C. Kleinkort, M. Thurai, and B. M. Notaroš, 2017: Dual-polarized radar and surface observations of a winter graupel shower with negative Z_{dr} column. *J. Appl. Meteor. Climatol.*, **56**, 455–470, https://doi.org/10.1175/JAMC-D-16-0197.1.

Browning, K. A., and C. D. Watkins, 1970: Observations of clear air turbulence by high power radar. *Nature*, **227**, 260–263, https://doi.org/10.1038/227260a0.

——, J. H. Marsham, A. B. White, and J. C. Nicol, 2012: A case study of a large patch of billows surmounted by elevated convection. *Quart. J. Roy. Meteor. Soc.*, **138**, 1764–1773, https://doi.org/10.1002/qj.1908.

Cann, M. D., and K. Friedrich, 2020: The role of moisture pathways on snowfall amount and distribution in the Payette Mountains of Idaho. *Mon. Wea. Rev.*, **148**, 2033–2048, https://doi.org/10.1175/MWR-D-19-0350.1.

Conrick, R., C. F. Mass, and Q. Zhong, 2018: Simulated Kelvin–Helmholtz waves over terrain and their microphysical implications. *J. Atmos. Sci.*, **75**, 2787–2800, https://doi.org/10.1175/JAS-D-18-0073.1.

Constantin, J. G., M. M. Gianetti, M. P. Longinotti, and H. R. Corti, 2018: The quasi-liquid layer of ice revisited: The role of temperature gradients and tip chemistry in AFM studies. *Atmos. Chem. Phys.*, **18**, 14 965–14 978, https://doi.org/10.5194/acp-18-14965-2018.

Durran, D. R., and J. B. Klemp, 1982: On the effects of moisture on the Brunt–Väisälä frequency. *J. Atmos. Sci.*, **39**, 2152–2158, https://doi.org/10.1175/1520-0469(1982)039<2152:OTEOMO>2.0.CO;2.

Ewing, G. E., 2004: Thin film water. *J. Phys. Chem.*, **108B**, 15 953–15 961, https://doi.org/10.1021/jp040378+.

Faber, S., J. R. French, and R. Jackson, 2018: Laboratory and in-flight evaluation of measurement uncertainties from a commercial Cloud Droplet Probe (CDP). *Atmos. Meas. Tech.*, **11**, 3645–3659, https://doi.org/10.5194/amt-11-3645-2018.

Finlon, J. A., G. M. McFarquhar, R. M. Rauber, D. M. Plummer, B. F. Jewett, D. Leon, and K. R. Knupp, 2016: A comparison of X-band polarization parameters with in situ microphysical measurements in the comma head of two winter cyclones. *J. Appl. Meteor. Climatol.*, **55**, 2549–2574, https://doi.org/10.1175/JAMC-D-16-0059.1.

Friedrich, K., D. E. Kingsmill, C. Flamant, H. V. Murphey, and R. M. Wakimoto, 2008: Kinematic and moisture characteristics of a nonprecipitating cold front observed during IHOP. Part II: Along front structures. *Mon. Wea. Rev.*, **136**, 3796–3821, https://doi.org/10.1175/2008MWR2360.1.

——, E. A. Kalina, J. Aikins, M. Steiner, D. Gochis, P. A. Kucera, K. Ikeda, and J. Sun, 2016: Raindrop size distribution and rain characteristics during the 2013 Great Colorado Flood. *J. Hydrometeor.*, **17**, 53–72, https://doi.org/10.1175/JHM-D-14-0184.1.

——, and Coauthors, 2020: Quantifying snowfall from orographic cloud seeding. *Proc. Natl. Acad. Sci. USA*, **117**, 5190–5195, https://doi.org/10.1073/pnas.1917204117.

Geerts, B., and Q. Miao, 2010: Vertically pointing airborne Doppler radar observations of Kelvin–Helmholtz billows. *Mon. Wea. Rev.*, **138**, 982–986, https://doi.org/10.1175/2009MWR3212.1.

Gourley, J. J., P. Tabary, and J. Parent du Chatelet, 2007: A fuzzy logic algorithm for the separation of precipitating from nonprecipitating echoes using polarimetric radar observations. *J. Atmos. Oceanic Technol.*, **24**, 1439–1451, https://doi.org/10.1175/JTECH2035.1.

Grasmick, C., and B. Geerts, 2020: Detailed dual-Doppler structure of Kelvin–Helmholtz waves from an airborne profiling radar over complex terrain. Part I: Dynamic structure. *J. Atmos. Sci.*, **77**, 1761–1782, https://doi.org/10.1175/JAS-D-19-0108.1.

Hallett, J., and S. C. Mossop, 1974: Production of secondary ice particles during the riming process. *Nature*, **249**, 26–28, https://doi.org/10.1038/249026a0.

Hosler, C. L., and R. E. Hallgren, 1960: The aggregation of small ice crystals. *Discuss. Faraday Soc.*, **30**, 200–206, https://doi.org/10.1039/df9603000200.

Houser, J. L., and H. B. Bluestein, 2011: Polarimetric Doppler radar observations of Kelvin–Helmholtz waves in a winter storm. *J. Atmos. Sci.*, **68**, 1676–1702, https://doi.org/10.1175/2011JAS3566.1.

Houze, R. A., and S. Medina, 2005: Turbulence as a mechanism for orographic precipitation enhancement. *J. Atmos. Sci.*, **62**, 3599–3623, https://doi.org/10.1175/JAS3555.1.

Hughes, M., A. Hall, and R. G. Fovell, 2009: Blocking in areas of complex topography, and its influence on rainfall distribution. *J. Atmos. Sci.*, **66**, 508–518, https://doi.org/10.1175/2008JAS2689.1.

Jackson, R. C., G. M. McFarquhar, J. Stith, M. Beals, R. A. Shaw, J. Jensen, J. Fugal, and A. Korolev, 2014: An assessment of the impact of antishattering tips and artifact removal techniques on cloud ice size distributions measured by the 2D cloud probe. *J. Atmos. Oceanic Technol.*, **31**, 2567–2590, https://doi.org/10.1175/JTECH-D-13-00239.1.

Jaeger, E. B., and M. Sprenger, 2007: A Northern Hemispheric climatology of indices for clear air turbulence in the tropopause region derived from ERA40 reanalysis data. *J. Geophys. Res.*, **112**, D20106, https://doi.org/10.1029/2006JD008189.

Keeler, J. M., R. M. Rauber, B. F. Jewett, G. M. McFarquhar, R. M. Rasmussen, L. Xue, C. Liu, and G. Thompson, 2017: Dynamics of cloud-top generating cells in winter cyclones. Part III: Shear and convective organization. *J. Atmos. Sci.*, **74**, 2879–2897, https://doi.org/10.1175/JAS-D-16-0314.1.

Keller, J. L., 1990: Clear air turbulence as a response to meso- and synoptic-scale dynamic processes. *Mon. Wea. Rev.*, **118**, 2228–2243, https://doi.org/10.1175/1520-0493(1990)118<2228:CATAAR>2.0.CO;2.

Kennedy, P. C., and S. A. Rutledge, 2011: S-band dual-polarization radar observations of winter storms. *J. Appl. Meteor. Climatol.*, **50**, 844–858, https://doi.org/10.1175/2010JAMC2558.1.

Kirshbaum, D. J., and D. R. Durran, 2004: Factors governing cellular convection in orographic precipitation. *J. Atmos. Sci.*, **61**, 682–698, https://doi.org/10.1175/1520-0469(2004)061<0682:FGCCIO>2.0.CO;2.

Knollenberg, R. G., 1970: The optical array: An alternative to scattering or extinction for airborne particle size determination. *J. Appl. Meteor. Climatol.*, **9**, 86–103, https://doi.org/10.1175/1520-0450(1970)009<0086:TOAAAT>2.0.CO;2.

Korolev, A. V., and I. P. Mazin, 2003: Supersaturation of water vapor in clouds. *J. Atmos. Sci.*, **60**, 2957–2974, https://doi.org/10.1175/1520-0469(2003)060<2957:SOWVIC>2.0.CO;2.

——, J. W. Strapp, G. A. Isaac, and A. N. Nevzorov, 1998: The Nevzorov airborne hot-wire LWC–TWC probe: Principle of operation and performance characteristics. *J. Atmos. Oceanic Technol.*, **15**, 1495–1510, https://doi.org/10.1175/1520-0426(1998)015<1495:TNAHWL>2.0.CO;2.

——, ——, G. A. Isaac, and E. Emery, 2013: Improved airborne hot-wire measurements of ice water content in clouds. *J. Atmos. Oceanic Technol.*, **30**, 2121–2131, https://doi.org/10.1175/JTECH-D-13-00007.1.

Kumjian, M. R., 2013a: Principles and applications of dual-polarization weather radar. Part I: Description of the polarimetric radar variables. *J. Operat. Meteor.*, **1**, 226–242, https://doi.org/10.15191/nwajom.2013.0119.

——, 2013b: Principles and applications of dual-polarization weather radar. Part II: Warm- and cold-season applications. *J. Operat. Meteor.*, **1**, 243–264, https://doi.org/10.15191/nwajom.2013.0120.

——, S. A. Rutledge, R. M. Rasmussen, P. C. Kennedy, and M. Dixon, 2014: High-resolution polarimetric radar observations of snow-generating cells. *J. Appl. Meteor. Climatol.*, **53**, 1636–1658, https://doi.org/10.1175/JAMC-D-13-0312.1.

Lalas, D. P., and F. Einaudi, 1974: On the correct use of the wet adiabatic lapse rate in stability criteria of a saturated atmosphere. *J. Appl. Meteor.*, **13**, 318–324, https://doi.org/10.1175/1520-0450(1974)013<0318:OTCUOT>2.0.CO;2.

Lance, S., C. A. Brock, D. Rogers, and J. A. Gordon, 2010: Water droplet calibration of the Cloud Droplet Probe (CDP) and in-flight performance in liquid, ice and mixed-phase clouds during ARCPAC. *Atmos. Meas. Tech.*, **3**, 1683–1706, https://doi.org/10.5194/amt-3-1683-2010.

Lawson, R. P., D. O'Connor, P. Zmarzly, K. Weaver, B. Baker, Q. Mo, and H. Jonsson, 2006: The 2D-S (Stereo) probe: Design and preliminary tests of a new airborne, high-speed, high-resolution particle imaging probe. *J. Atmos. Oceanic Technol.*, **23**, 1462–1477, https://doi.org/10.1175/JTECH1927.1.

Leon, D., and G. Vali, 1998: Retrieval of three-dimensional particle velocity from airborne Doppler radar data. *J. Atmos. Oceanic Technol.*, **15**, 860–870, https://doi.org/10.1175/1520-0426(1998)015<0860:ROTDPV>2.0.CO;2.

Libbrecht, K. G., 2005: The physics of snow crystals. *Rep. Prog. Phys.*, **68**, 855–895, https://doi.org/10.1088/0034-4885/68/4/R03.

Löffler-Mang, M., and J. Joss, 2000: An optical disdrometer for measuring size and velocity of hydrometeors. *J. Atmos. Oceanic Technol.*, **17**, 130–139, https://doi.org/10.1175/1520-0426(2000)017<0130:AODFMS>2.0.CO;2.

——, M. Kunz, and W. Schmid, 1999: On the performance of a low-cost Ka-band Doppler radar for quantitative rain measurements. *J. Atmos. Oceanic Technol.*, **16**, 379–387, https://doi.org/10.1175/1520-0426(1999)016<0379:OTPOAL>2.0.CO;2.

Maahn, M., and P. Kollias, 2012: Improved micro rain radar snow measurements using Doppler spectra post-processing. *Atmos. Meas. Tech.*, **5**, 2661–2673, https://doi.org/10.5194/amt-5-2661-2012.

Mahalov, A., M. Moustaoui, and V. Grubisic, 2011: A numerical study of mountain waves in the upper troposphere and lower stratosphere. *Atmos. Chem. Phys.*, **11**, 5123–5139, https://doi.org/10.5194/acp-11-5123-2011.

Majewski, A., and J. R. French, 2020: Supercooled drizzle development in response to semi-coherent vertical velocity fluctuations within an orographic-layer cloud. *Atmos. Chem. Phys.*, **20**, 5035–5054, https://doi.org/10.5194/acp-20-5035-2020.

Marsham, J. H., K. A. Browning, J. C. Nicol, D. J. Parker, E. G. Norton, A. M. Blyth, U. Corsmeier, and F. M. Perry, 2010: Multi-sensor observations of a wave beneath an impacting rear-inflow jet in an elevated mesoscale convective system. *Quart. J. Roy. Meteor. Soc.*, **136**, 1788–1812, https://doi.org/10.1002/qj.669.

Medina, S., and R. A. Houze Jr., 2016: Kelvin–Helmholtz waves in extratropical cyclones passing over mountain ranges. *Quart. J. Roy. Meteor. Soc.*, **142**, 1311–1319, https://doi.org/10.1002/qj.2734.

Miles, J. W., and L. N. Howard, 1964: Note on a heterogeneous shear flow. *J. Fluid Mech.*, **20**, 331–336, https://doi.org/10.1017/S0022112064001252.

Mitchell, D. L., 1996: Use of mass- and area-dimensional power laws for determining precipitation particle terminal velocities. *J. Atmos. Sci.*, **53**, 1710–1723, https://doi.org/10.1175/1520-0469(1996)053,1710:UOMAAD.2.0.CO;2.

Oue, M., M. R. Kumjian, Y. Lu, Z. Jiang, E. E. Clothiaux, J. Verlinde, and K. Aydin, 2015: X-band polarimetric and Ka-band Doppler spectral radar observations of a graupel-producing arctic mixed-phase cloud. *J. Appl. Meteor. Climatol.*, **54**, 1335–1351, https://doi.org/10.1175/JAMC-D-14-0315.1.

Petre, J. M., and J. Verlinde, 2004: Cloud radar observations of Kelvin–Helmholtz instability in a Florida anvil. *Mon. Wea. Rev.*, **132**, 2520–2523, https://doi.org/10.1175/1520-0493(2004)132<2520:CROOKI>2.0.CO;2.

Plummer, D. M., G. M. McFarquhar, R. M. Rauber, B. F. Jewett, and D. C. Leon, 2014: Structure and statistical analysis of the microphysical properties of generating cells in the comma head region of continental winter cyclones. *J. Atmos. Sci.*, **71**, 4181–4203, https://doi.org/10.1175/JAS-D-14-0100.1.

Rauber, R. M., and Coauthors, 2015: The role of cloud-top generating cells and boundary layer circulations in the finescale radar structure of a winter cyclone over the Great Lakes. *Mon. Wea. Rev.*, **143**, 2291–2318, https://doi.org/10.1175/MWR-D-14-00350.1.

Rauber, B., and Coauthors, 2019: Wintertime orographic cloud seeding – A review. *J. Appl. Meteor. Climatol.*, **58**, 2117–2140, https://doi.org/10.1175/JAMC-D-18-0341.1.

Ryzhkov, A. V., and D. S. Zrnić, 1998: Discrimination between rain and snow with a polarimetric radar. *J. Appl. Meteor.*, **37**, 1228–1240, https://doi.org/10.1175/1520-0450(1998)037<1228:DBRASW>2.0.CO;2.

Schneebeli, M., N. Dawes, M. Lehning, and A. Berne, 2013: High-resolution vertical profiles of X-band polarimetric radar observables during snowfall in the Swiss Alps. *J. Appl. Meteor. Climatol.*, **52**, 378–394, https://doi.org/10.1175/JAMC-D-12-015.1.

Schrom, R. S., and M. R. Kumjian, 2016: Connecting microphysical processes in Colorado winter storms with vertical profiles of radar observations. *J. Appl. Meteor. Climatol.*, **55**, 1771–1787, https://doi.org/10.1175/JAMC-D-15-0338.1.

——, ——, and Y. Lu, 2015: Polarimetric radar signatures of dendritic growth zones within Colorado winter storms. *J. Appl. Meteor. Climatol.*, **54**, 2365–2388, https://doi.org/10.1175/JAMC-D-15-0004.1.

Tessendorf, S. A., and Coauthors, 2019: A transformational approach to winter orographic weather modification research: The SNOWIE project. *Bull. Amer. Meteor. Soc.*, **100**, 71–92, https://doi.org/10.1175/BAMS-D-17-0152.1.

Trier, S. B., R. D. Sharman, and T. P. Lane, 2012: Influences of moist convection on a cold-season outbreak of Clear-Air Turbulence (CAT). *Mon. Wea. Rev.*, **140**, 2477–2496, https://doi.org/10.1175/MWR-D-11-00353.1.

Trömel, S., A. V. Ryzhkov, B. Hickman, K. Mühlbauer, and C. Simmer, 2019: Polarimetric radar variables in the layers of melting and dendritic growth at X band—Implications for a nowcasting strategy in stratiform rain. *J. Appl. Meteor. Climatol.*, **58**, 2497–2522, https://doi.org/10.1175/JAMC-D-19-0056.1.

Turner, J. S., 1973: Buoyancy *Effects* in *Fluids*. Cambridge University Press, 367 pp., https://doi.org/10.1017/CBO9780511608827.

Wang, Z., and Coauthors, 2012: Single aircraft integration of remote sensing and in situ sampling for the study of cloud microphysics and dynamics. *Bull. Amer. Meteor. Soc.*, **93**, 653–668, https://doi.org/10.1175/BAMS-D-11-00044.1.

World Meteorological Organization, 2017: Fluctus. International Cloud Atlas, https://cloudatlas.wmo.int/en/clouds-supplementary-features-fluctus.html.

Yuter, S. E., and R. A. Houze, 1995: Three-dimensional kinematic and microphysical evolution of Florida cumulonimbus. Part II: Frequency distributions of vertical velocity, reflectivity, and differential reflectivity. *Mon. Wea. Rev.*, **123**, 1941–1963, https://doi.org/10.1175/1520-0493(1995)123<1941:TDKAME>2.0.CO;2.

Zeng, G., and K. Li, 2019: Quasi-liquid layer on ice and its effect on the confined freezing of porous materials. *Crystals*, **9**, 250, https://doi.org/10.3390/cryst9050250.